Accepted Manuscript

Title: Micro-voids quantification for damage prediction in warm forging of biocompatible alloys using 3D X-ray CT and RVE approach

Authors: X.Z. Lu, L.C. Chan

PII: S0924-0136(18)30125-0
DOI: https://doi.org/10.1016/j.jmatprotec.2018.03.020
Reference: PROTEC 15690

To appear in: *Journal of Materials Processing Technology*

Received date: 9-1-2018
Revised date: 23-3-2018
Accepted date: 24-3-2018

Please cite this article as: Lu XZ, Chan LC, Micro-voids quantification for damage prediction in warm forging of biocompatible alloys using 3D X-ray CT and RVE approach, *Journal of Materials Processing Tech.* (2010), https://doi.org/10.1016/j.jmatprotec.2018.03.020

Micro-voids quantification for damage prediction in warm forging of biocompatible alloys using 3D X-ray CT and RVE approach

X.Z. Lu, L.C. Chan*

Department of Industrial and Systems Engineering, The Hong Kong Polytechnic University, Hung Hom, Kowloon, Hong Kong S.A.R., China

*Corresponding author

Tel.: +852 2766 6634

Fax: +852 2766 6771

E-mail addresses: lc.chan@polyu.edu.hk

Graphical Abstract

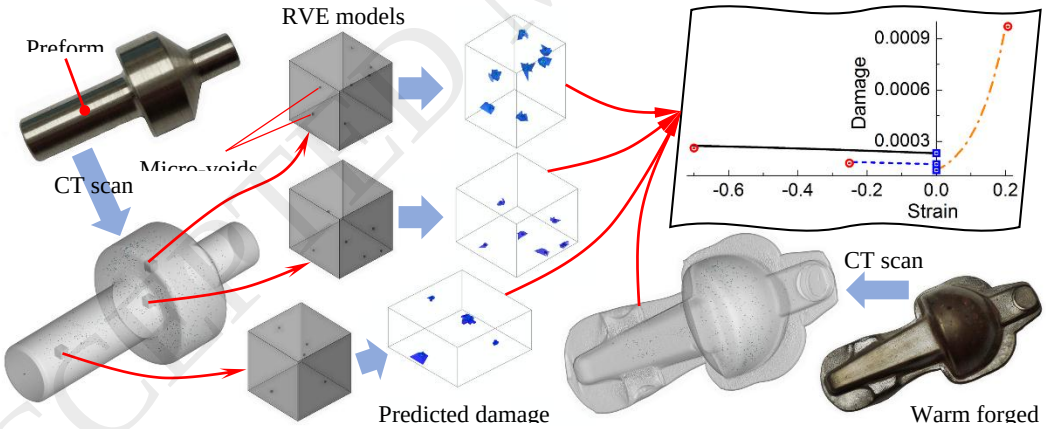

Abstract

This study aims to quantify the three-dimensional (3D) micro-voids for damage prediction in warm forging through non-destructive X-ray computed tomography (CT) and RVE approach. Typical biocompatible alloys, i.e., stainless steel 316L (SS316L) and titanium alloy Ti-6Al-4V, were used as specimen materials in warm-forging a medical implant, i.e., a basal thumb implant. X-ray CT scanning was performed for both the preforms and forged components. Volumetric CT images were then reconstructed and the 3D micro-void distribution and evolution inside the materials were detected and analysed quantitatively. Furthermore, three typical local strain regions, i.e., the small tensile strain region (STSR), small compressive strain region (SCSR) and large compressive strain region (LCSR), were established as the 3D representative volume element (RVE) models for both SS316L and Ti-6Al-4V preforms. The spatial location, size and volume of each micro-void were obtained from defect analysis of the 3D CT images and considered explicitly for subsequent damage prediction. An improved thermo-mechanical coupled micromechanics-based damage (micro-damage) model, which considered the variation of volume fraction of micro-voids (VFMVs), was implemented into finite element (FE) package ABAQUS for localized damage prediction of the RVE models. The damage distributions of the RVE models at different strain levels were visualized and identified. Finally, the localized damage evolutions at both compressive and tensile deformations were predicted and found to match quite well with the findings acquired from CT scanning. Thus, the application of non-destructive X-ray CT measurement of micro-voids,

incorporating the RVE approach, was able to play a significant role leading to a more reliable damage prediction in the warm forging process.

Keywords: Micro-voids; Damage prediction; Warm forging; Biocompatible alloys; X-ray computed tomography; Representative volume element.

1. Introduction

Due to the continual growth of the world's population, particularly the aging population, along with the maturation of medical technology, the demand for medical implants is ever-increasing. However, mechanical failures of metallic implants have been found, with an estimation of about 20% (Marshall et al., 2008). The main reason for this undesirable result arises from the manufacturing limitations of the fabrication processes, such as investment casting and metal injection molding, which inevitably leave voids and porosity inside the components (Boljanovic, 2009). In order to enhance the strength, and avoid sudden failure during the implantation of these critical metallic implants, warm forging is believed to be a viable alternative process (Sheljaskov, 1994). The forged component not only shows a more densified structure, less internal defects, and desirable grain flow strengthening, it also exhibits a better dimensional accuracy and surface quality over cast parts.

During the warm forging process, the inherent micro-defects (e.g., micro-voids/cracks, inclusions, etc.) can be reduced or healed under strong plastic compressive stress. However, some of the adjacent micro-defects may be aggregated and coalesced, which can lead eventually to damage accumulation and aggravation inside the component. Ishikawa et al. (2005) studied the causes of micro-defects initiation and found that it may not be possible to achieve defect-free components in general practice. Lee et al. (2011) predicted void deformation in forging large ingots and proposed a criterion for void closure. Chen and Lin (2013) investigated void evolution by FE simulations and experiments for large forgings during hot working.

Feng et al. (2016) conducted FE simulations of a 3D void growth model to investigate the internal void closure in the cogging process by considering the void shape, stress and strain state. It can be seen that the quantification of micro-voids to improve the constitutive models that account better for damage prediction is of great importance in the metal forming process.

Nowadays, the micromechanics-based damage (micro-damage) model is used widely for damage prediction due to the sound physical understanding of damage caused fundamentally by micro-void evolution in metallic material. Gurson (1977) originally proposed the void growth model based on the framework of micromechanics for porous materials. Tvergaard and Needleman (1984) extended Gurson's model for the FE analysis of cup-cone fracture through the initiation and evolution of voids, which is known as the GTN model. Pardoen and Hutchinson (2000) improved the GTN model to establish the criterion for the onset of coalescence by considering the void shape and location, strain hardening and stress triaxiality. By introducing two damage parameters, i.e., void volume fraction and shear growth parameter, Malcher et al. (2014) further extended the GTN model for ductile fracture prediction under different stress triaxiality conditions. Soyarslan et al. (2016) proposed a thermomechanical constitutive model which incorporated both micro-void and micro-crack for damage prediction at finite strains. Zhao et al. (2016) studied the damage mechanism of tearing failure in the fine-blanking process by combining the damage mechanics and the porous micromechanics model with consideration of the shear loading condition.

The above-mentioned damage models are always implemented in FE code for damage prediction. Since the micro-voids inside the metallic materials generally have irregular shapes and are distributed randomly, it is very difficult to describe all the microstructure details of the material at the macroscopic level and to carry out the FE simulation within reasonable computational time. Thus, multiscale analysis is booming as an effective method for investigating the material behaviour at different length scales (Geers et al., 2010). One of the most promising approaches for multiscale homogenization analysis is based on the concept of the representative volume element (RVE). By combining statistical analysis and numerical simulations, Gitman et al. (2007) determined the size of 2D RVE based on the Chi-square criterion for random heterogeneous material. Shen et al. (2009) investigated the influence of different shapes (sphere, triangular, rectangular, etc.) of defects on the effective Young's modulus of RVE. Lian et al. (2014) studied the damage initiation of DP steels on the microscopic level based on RVE simulations under different stress states. Chan et al. (2015) proposed a RVE-based multiscale approach for stress-strain behaviour prediction of void-considered metal alloy.

Although numerous studies of multiscale analysis have been done on various materials, the modelling of micro-voids in RVE is generally based on assumption or statistical analysis (Matouš et al., 2017), and the acquisition of damage parameters in FE simulations is obtained mostly through 2D destructive measurements (Zhao et al., 2016). This study, thus, aimed to incorporate the non-destructive X-ray CT with a 3D RVE approach for damage prediction in warm-forging biocompatible alloys. The

high-resolution X-ray CT detection enables the all-round visualization and quantification of the inherent micro-voids in three dimensions (Hsieh, 2009). For the CT scanning of material deformation at high temperatures, Kaye et al. (2013) viewed that the *in situ* measurement would result in the recrystallization of material during the interruption periods for CT image capturing. Therefore, *ex situ* X-ray CT scanning with a quenching process was adopted in this study to freeze the microstructure for better statistical analysis of the micro-void evolution during straining. Typical biocompatible alloys, stainless steel 316L (SS316L) and Ti alloy Ti-6Al-4V, were used in this study. The hot/warm forging temperature of austenitic SS316L had been carefully controlled and monitored within a very narrow range in order to avoid excessive grain growth or intergranular corrosion/cracking due to the hot cracking susceptibility (Matula et al., 2001). Whereas, hot/warm forging temperature range of titanium alloys is relatively wide, such as that Ti-6Al-4V alloy, which can be forged readily from 540 ºC to near β phase transition temperature (Park et al., 2002; Beal et al., 2006). Obviously, this is exactly the factual difference between that no phase change of mono-phase austenitic SS316L during hot/warm forging and that of hot-working on the two-phase (α+β) Ti-6Al-4V alloy (Momeni and Abbasi, 2010). A specific forging tooling was designed for warm-forging a basal thumb implant. Both the preforms and forged components were scanned and their volumetric CT images were reconstructed for quantitative analysis of the micro-void distribution. 3D RVE models representing different local strain conditions were then established and their

damage evolutions were predicted numerically with an improved thermo-mechanical coupled micro-damage model and further verified experimentally.

2. Experimental methods

2.1. Material and specimen preparation

The biocompatible alloys used in this study were cast SS316L and Ti-6Al-4V; their chemical compositions are shown in Table 1 and Table 2 respectively. The cast process leaves a variation in size of micro-voids and inclusions, which is conducive to subsequent micro-void measurement and analysis. Since the forging process involves applying compressive loading to a work piece, compression tests were carried out in this study to obtain the mechanical properties of the materials. The specimens for compression tests were cut to cylindrical shapes of Ø8.0mm×12.0mm. The configuration and dimensions of the basal thumb implant (Swanson, 2016) for warm forging experiments is shown in Fig. 1. Such a small component was conducive to the full penetration of an X-ray for the detection of the internal micro-voids, and it could be produced by the open-die forging process in one stroke. Since the spherical part of the implant was much bigger than the rod part, the preform was designed as a stepped cylinder, as shown in Fig. 2. The parting lines of the die were set at the maximum cross section area; flashes were formed at the parting lines after the die cavity was filled fully, and the external flash thickness was set as 0.8mm. It should be noted that the specimens used for compression tests and warm forging experiments were segmented from the same raw material to ensure the consistency of the material properties.

Table 1 Chemical composition (% in mass) of SS316L in this study.

C	Mn	S	Si	Cr	Ni	Mo	Fe
0.024	1.68	0.003	0.03	16.73	11.55	1.52	balance

Table 2 Chemical composition (% in mass) of Ti-6Al-4V in this study.

C	O	Fe	Al	V	Ti
0.03	0.03	0.25	6.22	4.15	balance

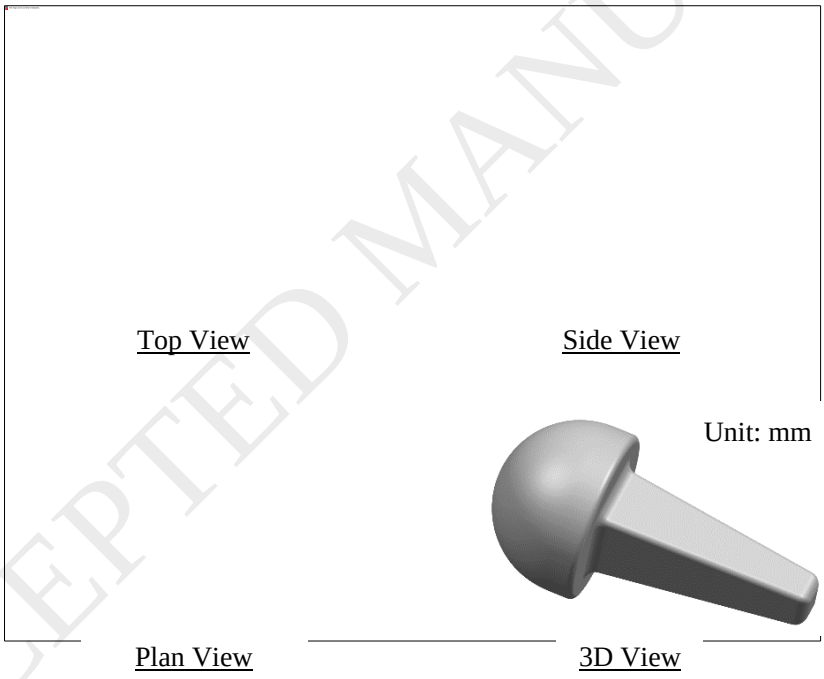

Fig. 1. The final configuration of a basal thumb implant in this study.

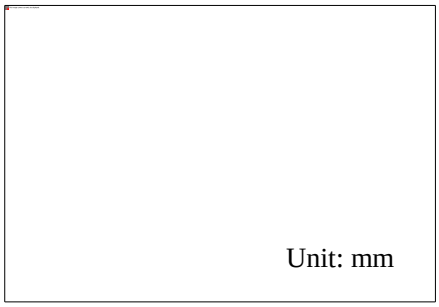

Fig. 2. The current design of the basal thumb implant preform.

2.2. X-ray CT scanning

A high-resolution micro-focus X-ray CT system YXLON FF35 CT was employed to detect the internal micro-void distributions of both the preforms and forged components. As an example, Fig. 3 shows the X-ray CT scanning of the forged basal thumb component. The X-ray tube source was operated at 160 kV voltage and 120 µA current for SS316L specimens as well as 140 kV voltage and 110 µA current for Ti-6Al-4V specimens. A tin sheet with a thickness of 1.0 mm was used as a pre-filter to reduce the beam hardening effect. 1440 projections were generated in one full rotation with a 400 ms integration time, and the 3D volumetric CT data were generated using the in-house CERA reconstruction spooler. Then the 2D and 3D CT images were visualized with VGStudio MAX 2.2. The comparison of relative pixel intensity values was adopted to separate the background and material in the CT images. An advanced segmentation algorithm was used for defect detection inside the specimen, which allowed for gray value variations, including noise reduction for seed point location and surrounding air connection. Hence, information like size, number,

spatial location, compactness, and sphericity of micro-voids could be obtained. An example for the micro-voids detection is shown in Fig. 4; it can be seen that this segmentation algorithm was able to identify different kinds of micro-voids inside the CT image accurately.

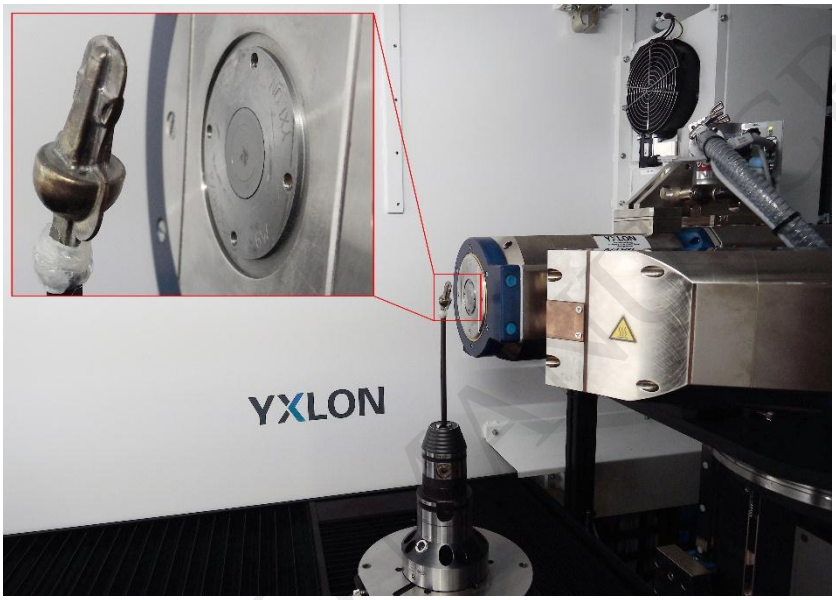

Fig. 3. X-ray CT scanning of the forged basal thumb component.

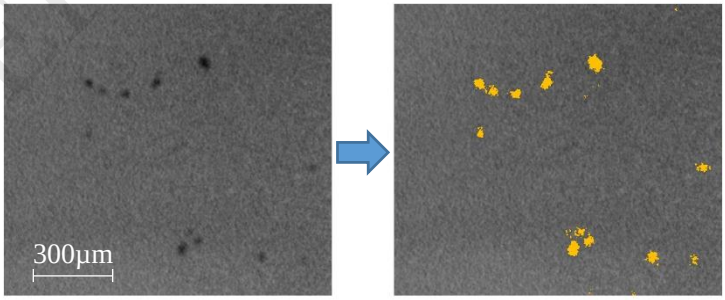

Fig. 4. Micro-voids detection: Original CT images on LHS; Constructed micro-voids in yellow via VGStudio on RHS.

2.3. Uniaxial compression tests and warm forging experiments

The uniaxial compression tests were conducted on an Gleeble 3500 thermal system. Typical warm forging temperatures for stainless steels and Ti-alloys, i.e., 800 ºC for SS316L and 700 ºC for Ti-6Al-4V, were chosen in this study. The strains were controlled at the rates of 0.001 s^{-1}, 0.01 s^{-1} and 0.1 s^{-1}, and the uniaxial compressive loading was gradually increased until a deformation of 50% was reached. During the test, the machine equipped with the computer processing system automatically recorded the relevant data, such as load-stroke and flow stress-strain, which were processed further to obtain the material parameters for FE simulations.

In addition, a specific forging tooling was designed for warm-forging the basal thumb implant. The tooling consisted mainly of die core components (upper and lower dies), heating and insulation devices, lift-up attachments and guide devices. They were installed on a self-developed forging system including a 160-ton AIDA mechanical press, a temperature controller, induction heating equipment, infrared thermometers and an infrared thermal camera, as shown in Fig. 5. Circular heaters were inserted into each die, enabling heating of the whole die set with the electric power supply to 250 °C, while the preform was heated by an induction heating device to the designated temperature and then placed into the lower die for forging with a speed of 20 SPM (stock per minute). The temperatures of the component and the tooling were monitored continuously by the infrared thermal camera to ensure an

accurate temperature control leading to a more reliable outcome of properties. Once forged, the component was taken out and quenched in water immediately to room temperature, thus to freeze the microstructure for the subsequent X-ray CT scanning.

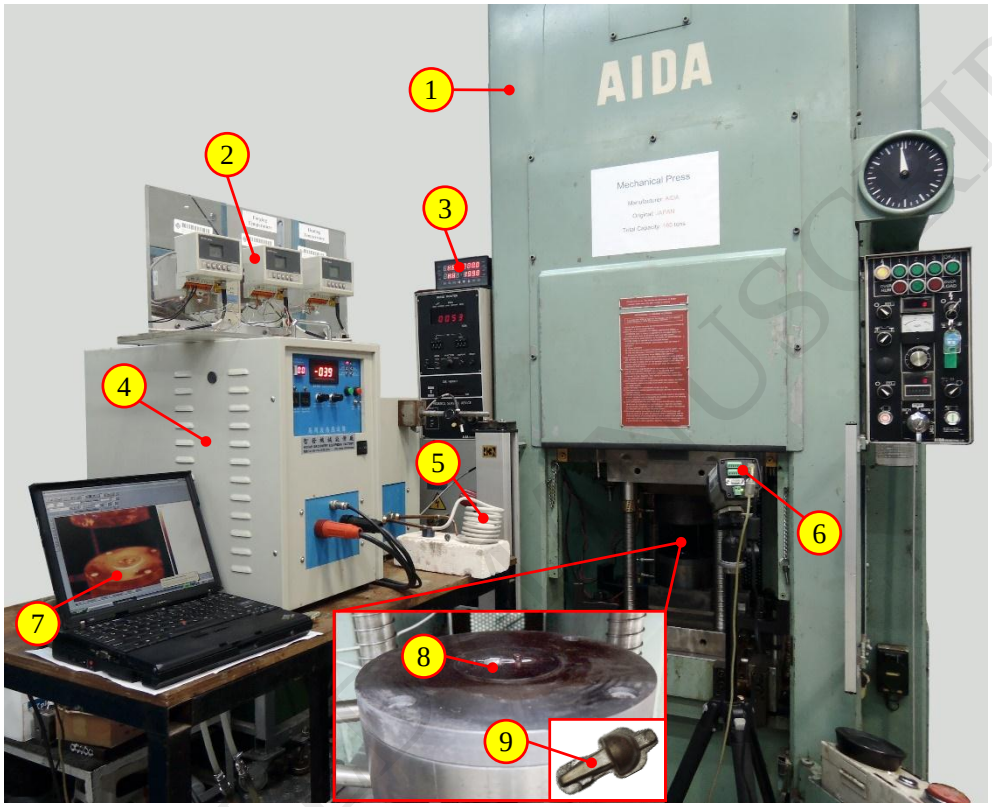

Fig. 5. A self-developed experimental system for warm-forging the basal thumb implant. Note: 1. 160T AIDA mechanical press; 2. Displays of the infrared thermometers for preform temperature measurement and monitoring; 3. Temperature monitor and controller for the forging die; 4. Induction heating equipment; 5. Preform inside the heating coil; 6. Infrared thermal camera; 7. Real-time temperature distribution during forging; 8. Bottom die core; 9. Forged component.

3. Thermo-mechanical coupled micro-damage model

During the warm forging process, the workpiece experiences plastic deformation and, at the same time, the temperature changes. The heat transfer between the workpiece and tooling, as well as the thermal radiation and convection between the workpiece and ambience, will result in a large temperature gradient in the forged component. The uneven distribution of temperature has a great influence on the mechanical properties of the material, which further influences the deformation process of the workpiece. Therefore, the interaction between deformation and heat transfer during the warm forging process should be considered. Thus, an improved thermo-mechanical coupled micro-damage model was presented in this study. Based on hypo-elastic relations, energy balance and entropy inequality (Zhu et al., 2016), the main equations for the thermo-mechanical coupled micro-damage model are described as follows.

3.1. Thermodynamic relationships

The Helmholtz free energy ψ is formulated as

$$\psi = \varphi - T\eta \tag{1}$$

where φ is the internal energy, T and η are the absolute temperature and entropy, respectively.

According to thermodynamics laws, the energy balance equation is expressed as

$$\frac{\boldsymbol{\tau}:\mathbf{D}}{\rho}-\dot{\psi}-\dot{T}\eta-\frac{J\nabla\mathbf{q}+r}{\rho}=T\dot{\eta} \tag{2}$$

and the dissipative inequality is given as

$$\frac{\boldsymbol{\tau}:\mathbf{D}}{\rho}-\dot{\psi}-\dot{T}\eta-J\frac{\mathbf{q}\cdot\nabla T}{\rho T}\geq 0 \tag{3}$$

where **D** is deformation rate tensor, $\boldsymbol{\tau}$ is Kirchhoff stress tensor, ρ is the specific density of a given material, *J* is the volume ratio (i.e., Jacobian determinant), ∇ is the vector differential operator, **q** represents the heat flux vector; *r* is the external heat source.

The intrinsic dissipation δ_{Int} and heat dissipation δ_{Heat} are defined as

$$\delta_{Int}=\frac{\boldsymbol{\tau}:\mathbf{D}}{\rho}-\dot{\psi}-\dot{T}\eta\ ,\quad \delta_{Heat}=-J\frac{\mathbf{q}\cdot\nabla T}{\rho T} \tag{4}$$

Generally, it is assumed that the heat flux **q** follows Fourier's law, i.e.,

$$\mathbf{q}=-k\mathbf{1}\cdot\nabla T \tag{5}$$

where *k* is the non-negative thermal conductivity coefficient, **1** is the second-order unit tensor.

To meet the requirement of the dissipation inequality, the intrinsic dissipation inequality should be non-negative, i.e.,

$$\delta_{Int}=\frac{\boldsymbol{\tau}:\mathbf{D}}{\rho}-\dot{\psi}-\dot{T}\eta\geq 0 \tag{6}$$

3.2. Constitutive equations

The deformation rate tensor **D** is decomposed into two parts

$$\mathbf{D}=\mathbf{D}^{e}+\mathbf{D}^{p} \tag{7}$$

where superscript e and p indicate the elastic and plastic parts, respectively.

According to Xiao et al. (2007), the elastic part of Hencky's strain $\mathbf{h}^{e}$ can be regarded as a state variable to formulate the constitutive equations, i.e.,

$$\mathbf{D}^{e} = \overset{\circ}{\mathbf{h}}^{\log(e)} \tag{8}$$

In this study, the concept of volume fraction of micro-voids *f* was introduced. The constitutive laws of ψ , $\boldsymbol{\tau}$, η and $\mathbf{q}$ are assumed to be the functions of independent variables $\left(\mathbf{h}^{e},\ f,T\right)$, i.e.,

$$\boldsymbol{\tau} = \hat{\boldsymbol{\tau}}\left(\mathbf{h}^{e},\ f,T\right) \tag{9a}$$

$$\psi = \hat{\psi}\left(\mathbf{h}^{e},\ f,T\right) \tag{9b}$$

$$\eta = \hat{\eta}\left(\mathbf{h}^{e},\ f,T\right) \tag{9c}$$

$$\mathbf{q} = \hat{\mathbf{q}}\left(\mathbf{h}^{e},\ f,T\right) \tag{9d}$$

Differentiating Eq. (9b) with respect to time, we can obtain

$$\dot{\psi} = \frac{\partial \hat{\psi}}{\partial \mathbf{h}^{e}} : \dot{\mathbf{h}}^{e} + \frac{\partial \hat{\psi}}{\partial f}\dot{f} + \frac{\partial \hat{\psi}}{\partial T}\dot{T} \tag{10}$$

If the material is restricted to the initial isotropic, and the function Eq. (9b) is assumed as a quadratic form, Eq. (10) can be rewritten as

$$\dot{\psi} = \frac{\partial \hat{\psi}}{\partial \mathbf{h}^{e}} : \mathbf{D} - \frac{\partial \hat{\psi}}{\partial \mathbf{h}^{e}} : \mathbf{D}^{p} + \frac{\partial \hat{\psi}}{\partial f}\dot{f} + \frac{\partial \hat{\psi}}{\partial T}\dot{T} \tag{11}$$

Substitute Eq. (11) into the intrinsic dissipation inequality (Eq. (6)) gives

$$\left(\frac{\boldsymbol{\tau}}{\rho} - \frac{\partial \hat{\psi}}{\partial \mathbf{h}^{e}}\right) : \mathbf{D} - \left(\eta + \frac{\partial \hat{\psi}}{\partial T}\right)\dot{T} + \frac{\partial \hat{\psi}}{\partial \mathbf{h}^{e}} : \mathbf{D}^{p} + \frac{\partial \hat{\psi}}{\partial f}\dot{f} \geq 0 \tag{12}$$

According to the Coleman-Noll procedure (Coleman and Noll, 1963), Eq. (12) is meaningful for any thermodynamic process, which indicates that the coefficients, $\frac{\boldsymbol{\tau}}{\rho} - \frac{\partial \hat{\psi}}{\partial \mathbf{h}^{\mathrm{e}}}$ and $\eta + \frac{\partial \hat{\psi}}{\partial T}$ for variables $\mathbf{D}$ and $\dot{T}$ respectively, must be zero. Hence the following constitutive equations are obtained

$$\boldsymbol{\tau} = \rho \frac{\partial \hat{\psi}}{\partial \mathbf{h}^{\mathrm{e}}} \tag{13a}$$

$$\eta = -\frac{\partial \hat{\psi}}{\partial T} \tag{13b}$$

By defining

$$F_f = \frac{\partial \hat{\psi}}{\partial f} \tag{14}$$

The Eq. (12) can be reformulated as

$$\frac{\boldsymbol{\tau} : \mathbf{D}^{\mathrm{p}}}{\rho} + F_f \dot{f} \geq 0 \tag{15}$$

Hence the intrinsic dissipation δ_{Int} is given as

$$\delta_{Int} = \frac{\boldsymbol{\tau} : \mathbf{D}^{\mathrm{p}}}{\rho} + F_f \dot{f} \tag{16}$$

Combining the Eqs. (4), (13) and (16), the Eq. (2) can be written as

$$\frac{\boldsymbol{\tau} : \mathbf{D}^{\mathrm{p}}}{\rho} + \frac{Jk\nabla^2 T + r}{\rho} = -T\left(\frac{\partial \boldsymbol{\tau}}{\partial T} : \mathbf{D}^{\mathrm{e}} + \frac{\partial F_f}{\partial T}\dot{f} + \frac{\partial^2 \hat{\psi}}{\partial T^2}\dot{T}\right) \tag{17}$$

Normally, the specific heat is given as

$$c = -T\frac{\partial^2 \hat{\psi}}{\partial T^2} = \hat{c}\left(\mathbf{h}^{\mathrm{e}}, T\right) \tag{18}$$

Then the heat conduction equation is finally obtained as

$$\underbrace{\frac{\boldsymbol{\tau}:\mathbf{D}^{\mathrm{p}}}{\rho}}_{\text{Inelastic heat}}+\underbrace{T\frac{\partial\boldsymbol{\tau}}{\partial T}:\mathbf{D}^{\mathrm{e}}}_{\text{Elastic heat}}+\frac{\partial F_f}{\partial T}\dot{f}+\underbrace{Jk\nabla^2 T}_{\text{Heat flux}}+\underbrace{r}_{\text{External heat}}=c\dot{T} \tag{19}$$

As shown in Eq. (19), the terms $\frac{\boldsymbol{\tau}:\mathbf{D}^{\mathrm{p}}}{\rho}$ and $T\frac{\partial\boldsymbol{\tau}}{\partial T}:\mathbf{D}^{\mathrm{e}}$ denote inelastic and elastic heat respectively, $Jk\nabla^2 T$ is the heat flux; r is the external heat source which is usually negligible. Hence, the temperature field can be solved by Eq. (19) once the specific constitutive relations are given.

3.3. Specific form of constitutive equations

Referring to Rosakis et al. (2000), the specific heat c can be assumed to be independent of $\mathbf{h}^{\mathrm{e}}$, which implies that the Kirchhoff's stress tensor $\boldsymbol{\tau}$ is linear with respect to T. Assuming that the material is stress-free at the reference temperature T_0, the hypo-thermo-elastic relation is given as

$$\boldsymbol{\tau}=\rho\left(\mathbb{D}:\mathbf{h}^{\mathrm{e}}-3a\kappa\left(T-T_0\right)\mathbf{1}\right) \tag{20}$$

where $\mathbb{D}$ is the fourth-order elastic tensor, a is the thermal expansion coefficient, $\kappa=E/3(1-2\nu)$ is the bulk modulus (in which E and ν are elastic modulus and Poisson's ratio, respectively).

And the logarithmic rate of Kirchhoff stress tensor $\boldsymbol{\tau}$ can be expressed as

$$\overset{\circ}{\boldsymbol{\tau}}^{\log}=\rho\left(\mathbb{D}:\mathbf{D}^{\mathrm{e}}-3a\kappa\dot{T}\mathbf{1}\right) \tag{21}$$

The plastic deformation rate tensors $\mathbf{D}^{\mathrm{p}}$ can be decomposed into two parts, i.e., the deviatoric stress tensor $\mathbf{D}^{\mathrm{p}\prime}$ and the hydrostatic stress tensor $\mathbf{D}^{\mathrm{p(m)}}$,

$$\mathbf{D}^{p} = \mathbf{D}^{p\prime} + \mathbf{D}^{p(m)} = \mathbf{D}^{p\prime} + \frac{1}{3}\mathrm{tr}\left(\mathbf{D}^{p}\right)\mathbf{1} \tag{22}$$

According to Rousselier (2001), the visco-plastic flow rules of $\mathbf{D}^{p\prime}$ and $\mathrm{tr}\left(\mathbf{D}^{p}\right)$ can be assumed as

$$\mathbf{D}^{p\prime} = \sqrt{\frac{3}{2}}\dot{p}\mathbf{N} = \sqrt{\frac{3}{2}}\left\langle\frac{F_y}{K}\right\rangle^{n}\mathbf{N} \tag{23}$$

$$\mathrm{tr}\left(\mathbf{D}^{p}\right) = fs_1 \exp\left(\frac{\mathrm{tr}(\boldsymbol{\tau})}{3s_2\rho}\right)\dot{p} \tag{24}$$

where $\dot{p}$ is the accumulated plastic strain rate, n and K are the material viscosity constants. s_1 and s_2 are damage parameters, $\langle\ \rangle$ is the McCauley operator; $\mathbf{N} = \frac{\boldsymbol{\tau}'}{\|\boldsymbol{\tau}'\|}$ is the unit normal vector of the yield surface F_y.

The yield surface F_y can be formulated as

$$F_y = \sqrt{\frac{3}{2}}\left\|\boldsymbol{\tau}'/\rho\right\| + fs_1s_2\exp\left(\frac{\mathrm{tr}(\boldsymbol{\tau})}{3s_2\rho}\right) - Q \tag{25}$$

Based on the isotropic hardening rule, the deformation resistance Q consists of the initial resistance Q_0 and the subsequent resistance R, as

$$Q = Q_0 + R \tag{26}$$

The evolution of R can be expressed as

$$\dot{R} = \beta\left(R^{sat} - R\right)\dot{p} \tag{27}$$

where R^{sat} represents the saturated value of R during the compressive deformation, β is the evolution rate of R.

Based on the effective stress concept and mass conservation proposed by Rousselier (2001), the evolution law of the volume fraction of micro-voids *f* can be given as

$$\dot{f} = \rho \, \mathrm{tr}\left(\mathbf{D}^{p}\right) = \rho \, f s_1 \exp\left(\frac{\mathrm{tr}(\boldsymbol{\tau})}{3 s_2 \rho}\right) \dot{p} \tag{28}$$

The driving force is formulated as

$$F_f = \frac{s_2}{\rho_0} \ln\left(\frac{f(1-f_0)}{f_0(1-f)}\right) \tag{29}$$

4. Results and discussion

4.1. Experimental stress-strain curves

The uniaxial compressive stress-strain curves of cast SS316L at 800 ºC and Ti-6Al-4V at 700 ºC are shown in Fig. 6 and Fig. 7 respectively. It can be observed that the strain rate had little influence on the elastic modulus of the material at a specific temperature. However, a significant rate effect on the plastic deformation behaviour was found in both SS316L and Ti-6Al-4V, i.e., the increasing of strain rate led to significant increases in the yield and ultimate stresses of the material. After the ultimate stresses were reached, the plastic stress experienced a long stable region for the SS316L and declined gradually for the Ti-6Al-4V.

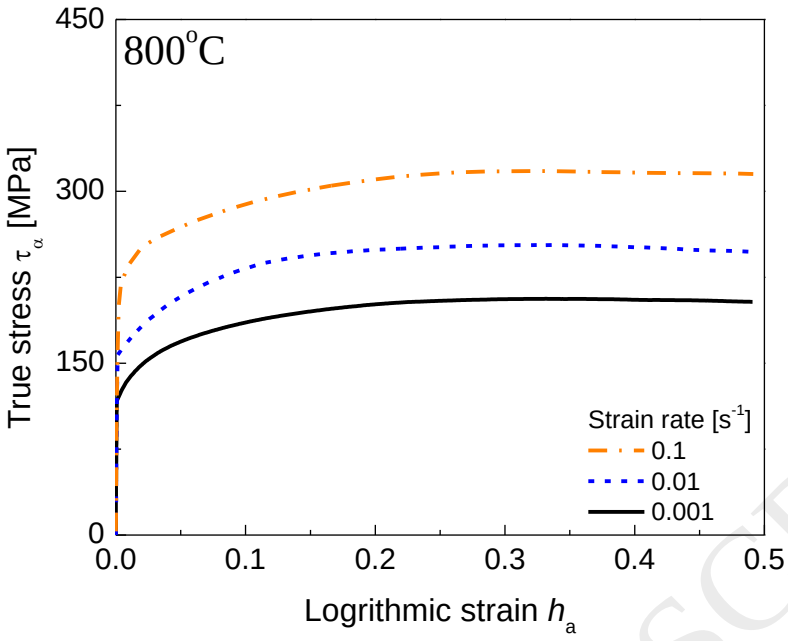

Fig. 6. Experimental compressive stress-strain curves of the SS316L specimens at elevated temperature of 800 ºC.

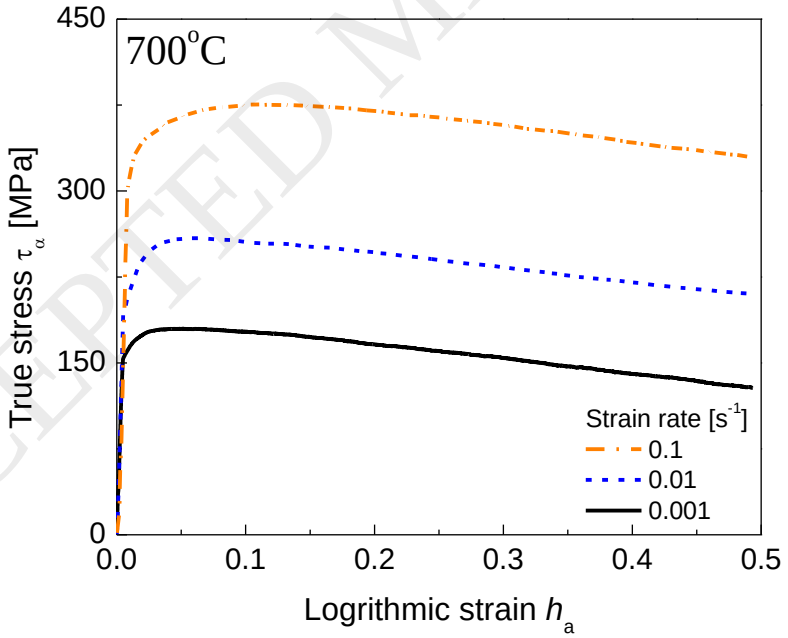

Fig. 7. Experimental compressive stress-strain curves of the Ti-6Al-4V specimens at elevated temperature of 700 ºC.

The material constants involved in the micro-damage model can be obtained through fitting the experimental stress-strain data; details about the identification of material parameters can be found in our published work (Lu and Chan, 2017). It should be noted that the parameters R^{sat} and β involved in Eq. (27) were extended to two terms for better fitting the declined parts of the stress-strain curves of Ti-6Al-4V. In addition, the thermal properties of these two materials are discussed in BSSA (2016) and Veiga et al. (2012) respectively. The determined material parameters are listed in Table 3.

Table 3 Material parameters of SS316L (at 800 ºC) and Ti-6Al-4V (at 700 ºC) to be involved in the formulation of thermo-mechanical coupled micro-damage model.

	E (GPa)	v	Q_0 (MPa)	R^{sat1} (MPa)	R^{sat2} (MPa)	β_1	β_2	K	n	s_1	s_2	c (J/kg.K)	k (W/m·K)
SS316L	134	0.24	120	84.7	/	16.5	/	300	6	2	200	628	21.0
Ti-6Al-4V	32	0.34	150	37.2	174	78.8	-0.6	500	5	2	235	750	14.6

4.2. CT image reconstruction and quantitative analysis of micro-void distribution and evolution in warm forging

With the aid of the in-house CERA reconstruction spooler, the CT images of the preforms and forged basal thumb components made of SS316L and Ti-6Al-4V were

reconstructed. The internal micro-voids were analysed quantitatively using the defect detection mode in VGStudio. The experimental preforms and forged components, as well as their 3D CT images with internal micro-voids, are shown in Fig. 8. The CT images were displayed semi-transparently to better reveal the distribution of internal micro-voids; the material is represented in grey and the micro-voids are represented in other colours. It can be seen that the micro-void distribution was not uniform throughout the specimen, and the volumes of the micro-voids varied a lot, indicating that the casting process left micro-voids randomly.

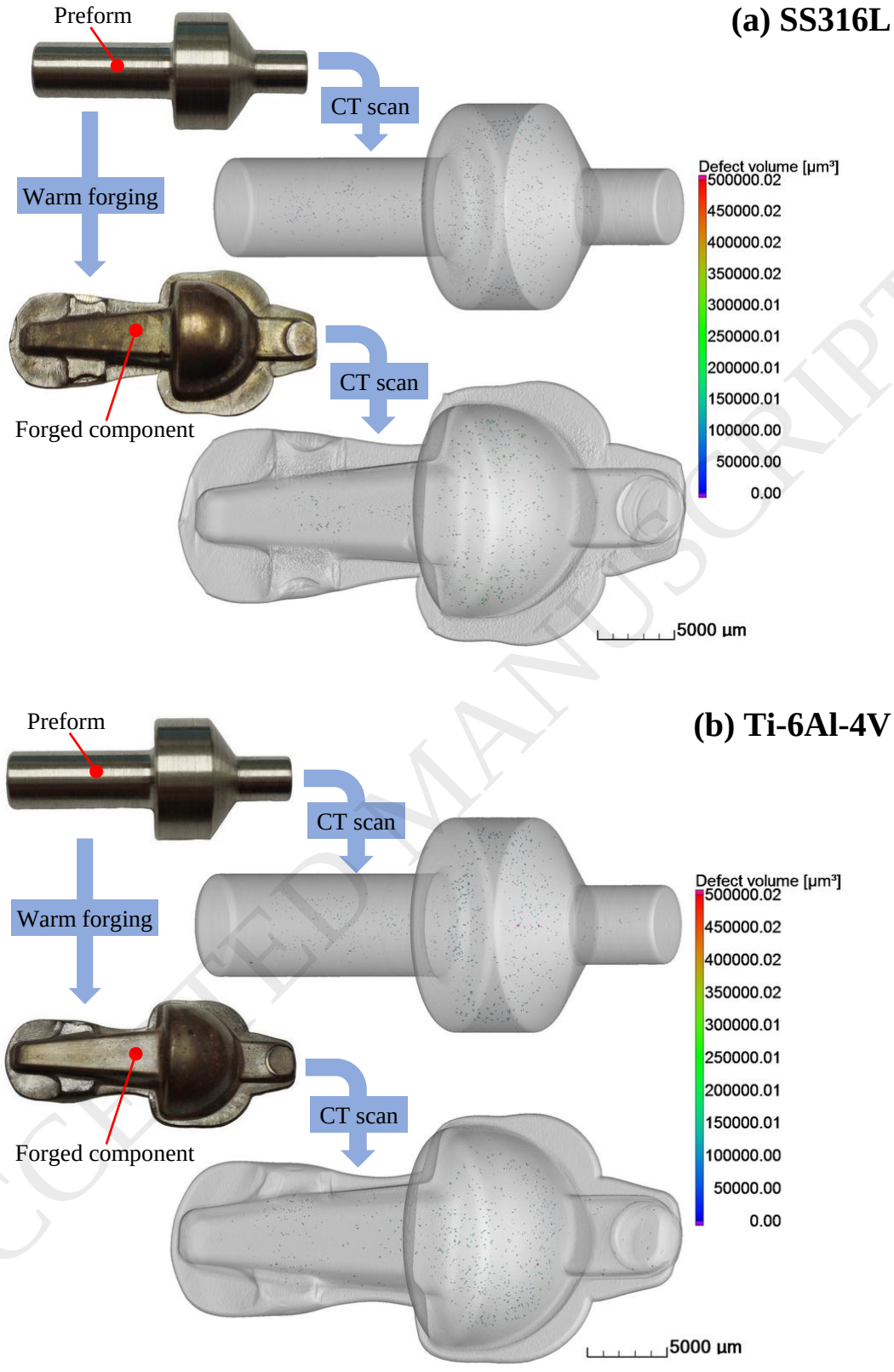

Fig. 8. The experimental preforms and forged components as well as their 3D CT images with internal micro-voids to be illustrated on (a) SS316L and (b) Ti-6Al-4V.

With 3D tomography, enough micro-voids were detected in three dimensions to ensure a meaningful statistical analysis of sizes, shapes and spatial locations of micro-voids. Fig. 9 shows the quantitative analysis of the size distribution of micro-voids for the SS316L and Ti-6Al-4V preforms. It can be seen that the size distribution of these two cast preforms were similar. More specifically, the sizes of the micro-voids inside the SS316L preform ranged from 22.2μm to 68.9μm with an average size of 33.5μm, and most of the micro-voids (approx. 87.7%) were sized between 28.7μm and 41.8μm. For the Ti-6Al-4V preform, the sizes of the micro-voids ranged from 23.4μm to 67.0μm with an average size of 33.3μm, while most of the micro-voids (approx. 91.3%) were sized between 24.5μm and 41.5μm.

Furthermore, the micro-void evolution after warm forging for these two kinds of materials were analysed (see Fig. 9). It can be seen that the maximum sizes and total number of micro-voids were reduced for both SS316L and Ti-6Al-4V after warm forging, while the average sizes of micro-voids were slightly increased to 35.8μm and 34.1μm for SS316L and Ti-6Al-4V respectively. However, the micro-void distributions of these two materials after warm forging were quite different. For SS316L, the small-sized micro-voids (i.e., <24.4μm) were healed after warm forging. The number of micro-voids ranged from 37.5μm to 43.4μm was increased after warm forging, which may be for the following two reasons: 1) the compressive force during warm forging reduced the size of the larger micro-voids (e.g., 50.0μm ~ 68.9μm) and thus increased the number of micro-voids in the size range of 37.5μm ~ 43.4μm; 2)

part of the adjacent medium-sized (e.g., 28.7μm ~ 33.7μm) micro-voids coalesced and thus their size increased. On the other hand, the size of most micro-voids was reduced and the number of small-sized micro-voids was increased for the forged Ti-6Al-4V component. Its size distribution indicated that the micro-voids were compressed gradually and void coalescence were hardly formed.

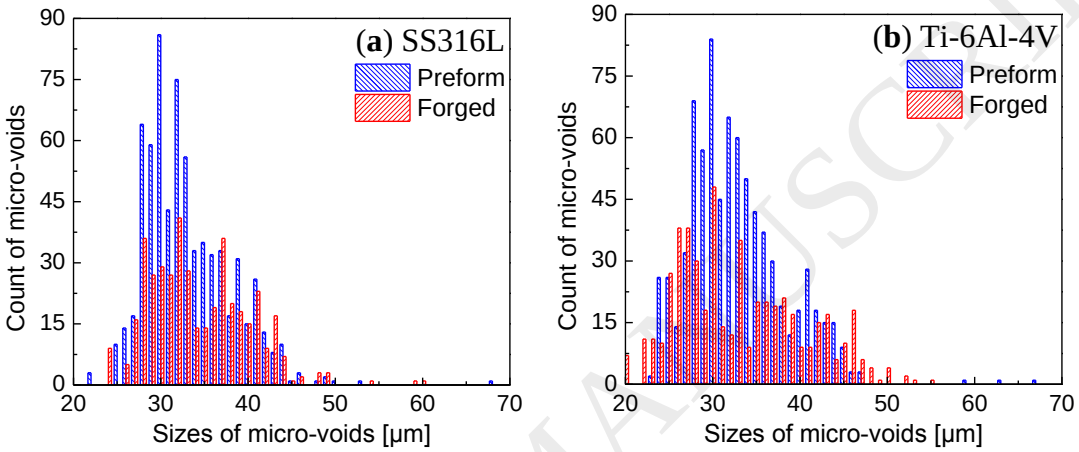

Fig. 9. Sizes distribution of micro-voids in: (a) SS316L and (b) Ti-6Al-4V.

4.3. Damage prediction in warm-forging the basal thumb implant and verification

In this study, FE simulations for warm-forging the basal thumb implant were carried out using the commercial package ABAQUS. Due to the complex shape of the component, the predicted stress and strain distributions in different regions of the forged component were varied considerably, as shown in Fig. 10. The comparison of temperature distributions between the FE prediction and thermal camera imaging of the forged SS316L component is shown in Fig. 11. It can be seen that the temperatures of most areas of the component were reduced. Feature points (P1~P6)

selected for the surface of the forged component showed that the predicted temperatures were close to the experimental values and the errors were within 5% (Fig. 11c), indicating that the thermo-mechanical coupled micro-damage model was able to predict the temperature field distribution during the warm forging process.

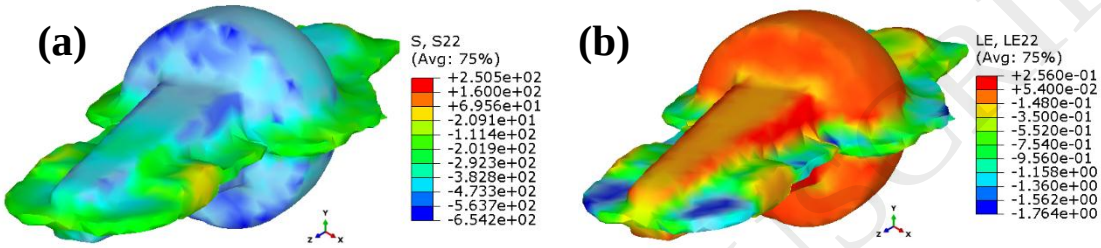

Fig. 10. The predicted stress distribution (a) and strain distribution (b) of the forged SS316L basal thumb component.

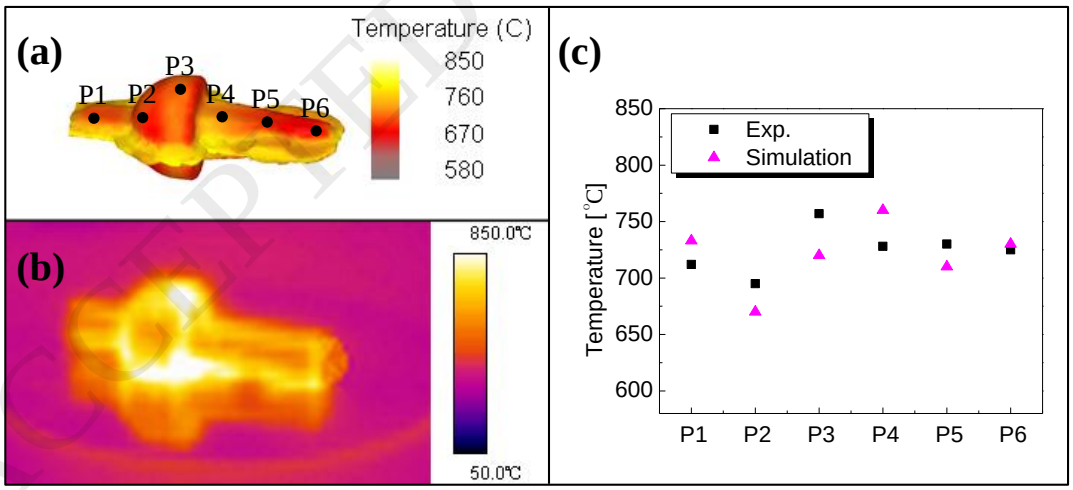

Fig. 11. Comparison of temperature distributions between (a) prediction and (b) thermal camera capturing image of the forged SS316L component, as well as (c) temperature comparison of selected feature points.

Since numerous micro-voids were detected from the preforms with random distribution and irregular shapes, it is a great challenge to model all the configurations of micro-voids accurately and to carry out the numerical simulation within a reasonable computational time. Therefore, several representative local regions of the preform were constructed as RVE models to study the damage evolution induced from micro-voids during the warm forging process. The varied stress and strain distributions in different regions of the forged component enabled us to analyse the damage evolution at different strain conditions in one forging process. Thus, three typical local strain regions, i.e., small tensile strain region (STSR), small compressive strain region (SCSR) and large compressive strain region (LCSR), were selected according to the strain distribution of the forged component, as shown in Fig. 12, whereas the simulated forged component was cut in half along the XY plane to better demonstrate its internal strain distribution.

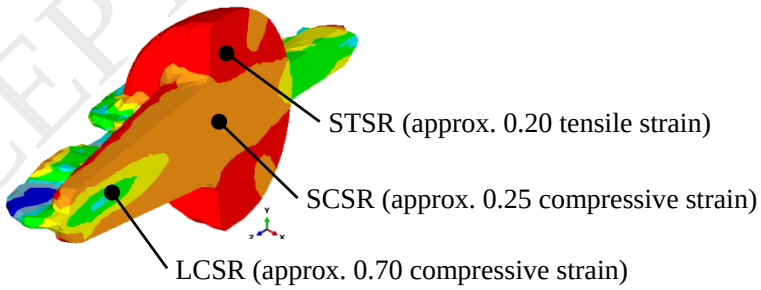

Fig. 12. Three typical strain regions of the forged SS316L basal thumb component: STSR, SCSR and LCSR.

Corresponding cuboid RVE models with side length of 1.0mm were constructed from the preform, as shown in Fig. 13. These RVE models included the information about the spatial location (X, Y, Z), diameter (in μm), and volume of each micro-void. Hence, the volume fraction of micro-voids (VFMV) could be obtained, i.e., the total volume of micro-voids inside the RVE divided by the volume of RVE. By simplifying the micro-voids into spherical shapes with the spatial location represented as the centre of the sphere, geometrical RVE models were then reconstructed for the subsequent damage prediction through FE simulations (see Fig. 13).

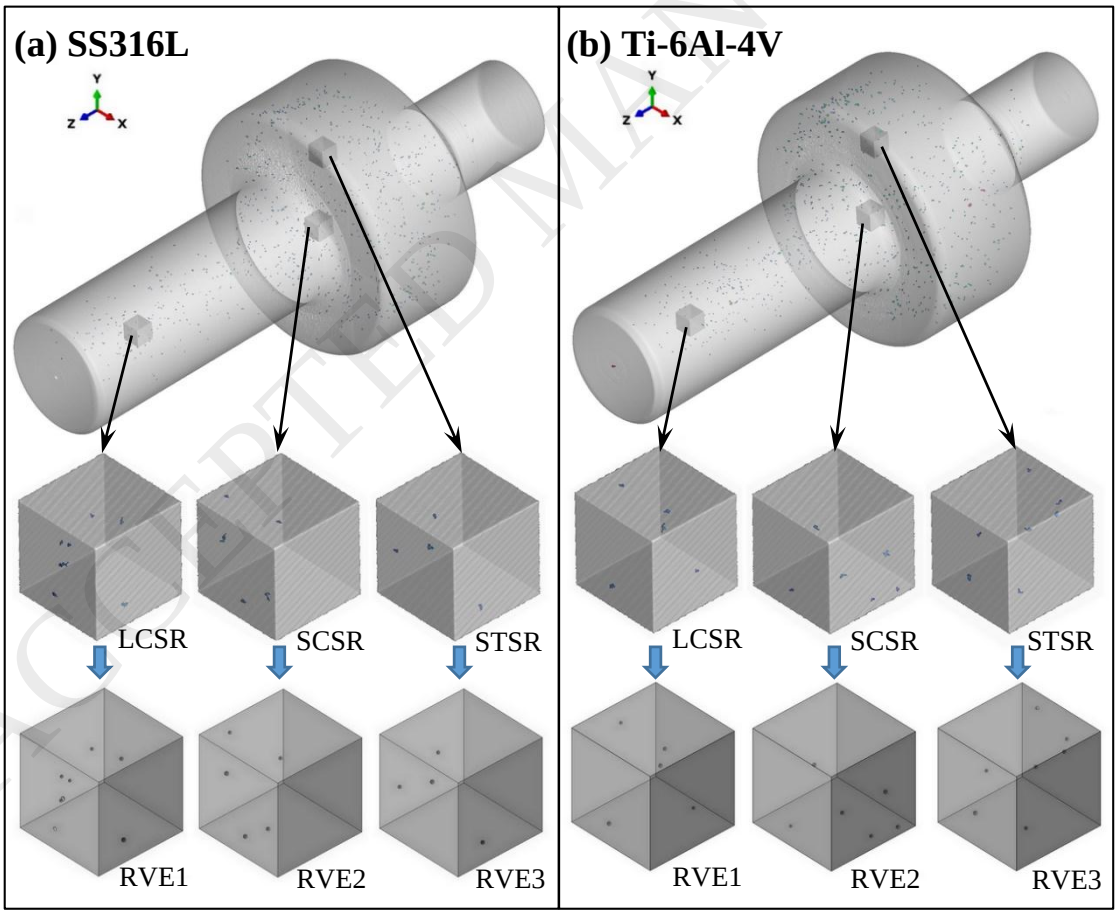

Fig. 13. RVE models (1.0mm in side length) constructed after CT scanning of the preforms: (a) SS316L and (b) Ti-6Al-4V.

For the FE simulations, the RVE models were meshed with 3D 4-node thermal coupled linear tetrahedron element (C3D4T). 800 ºC and 700 ºC were assigned as the warm forging temperatures for SS316L and Ti-6Al-4V RVE models respectively. Periodic boundary conditions were applied on the RVE models by adding coupled constraint equations in ABAQUS. Axial displacement in Y direction was imposed on the nodes of the top surface with the strain rate controlled by changing the total simulation time period. The thermo-mechanical coupled micro-damage model developed in Section 3, including the evolution laws of hypo-thermo-elastic relation (Eq. (20)), viscoplastic flow rules (Eqs. (23-24)), yield function (Eq. (25)) and volume fraction of micro-voids (Eq. (28)), was compiled and implemented into ABAQUS using a user defined material subroutine UMAT. The elastoplastic, thermal and damage parameters given in Table 3 were employed in the UMAT to model the material behaviour during the warm forging simulations.

The damage evolution of the RVE models under warm forging was predicted in this study. The variable SDV4 obtained from the simulations represents the predicted damage value, and its initial value is the VFMV of the RVE model. The changing of VFMV can be regarded as the damage evolution in the warm forging process, therefore, the values of VFMV obtained through CT scanning were used for the

verification of the predicted damage in subsequent FE simulations. The RVE1 of the SS316L preform, which was displayed semi-transparently, was selected as an example to visualize its internal damage distribution (see Fig. 14). It can be seen that the more severe damage was concentrated around the micro-voids, while the damage of the area away from the micro-voids was almost unchanged. By removing the elements with damage below a certain value, it was possible to visualize clearly the localized damage distribution in RVE models, as shown in Fig. 15. The results showed that the more severe damage was always distributed around the micro-voids, and the elements with more severe damage were less in both low and high compressive strain levels (for RVE1 and RVE2) and increased a lot in tensile strain conditions (for RVE3). This indicated that the damage evolved very slowly under compressive deformation, while it grew quickly under tensile deformation.

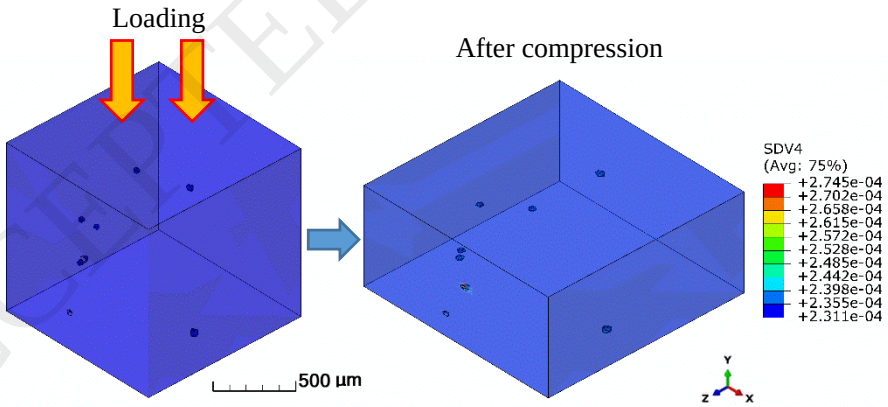

Fig. 14. Predicted damage distribution of RVE1 for SS316L (800 ºC, 0.1 s^{-1} strain rate, at strain of -0.70 (*LE22*)).

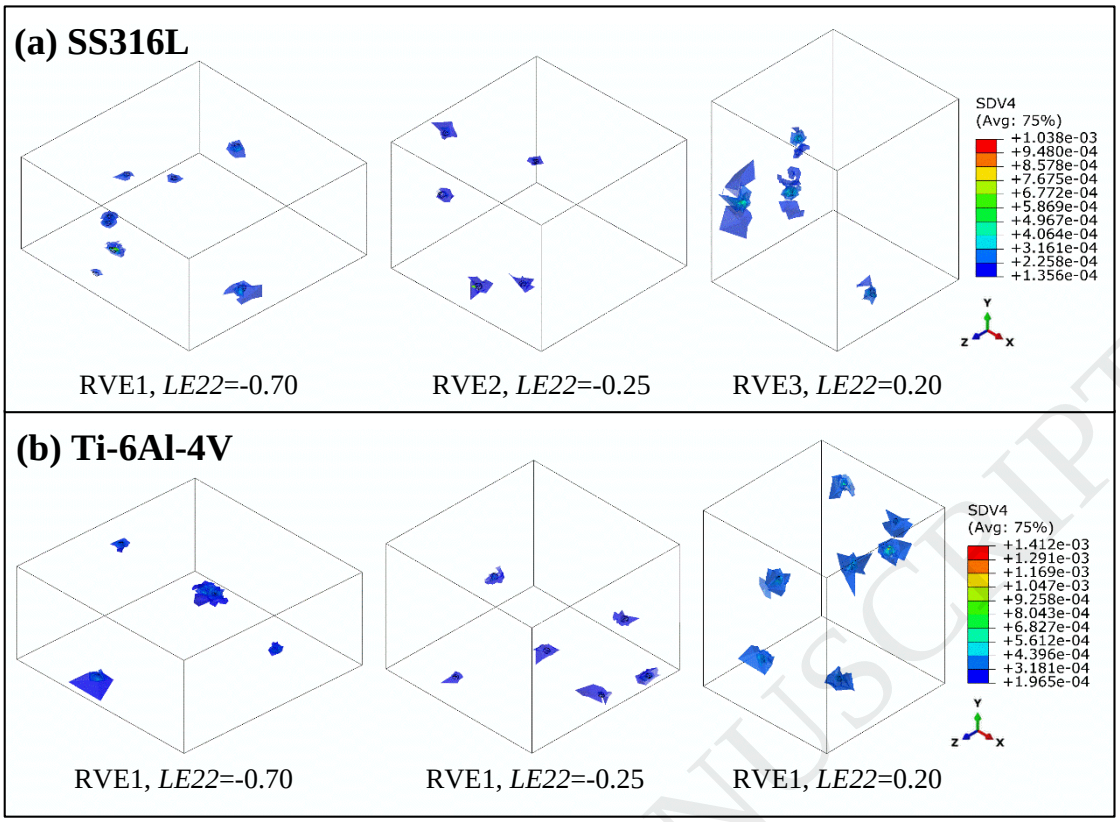

Fig. 15. Damage localization around the micro-voids in RVE models of (a) SS316L and (b) Ti-6Al-4V.

More specifically, the damage evolution at different strain levels for these RVE models is shown in Fig. 16. Since the numerical forming speed of the RVE models at the strain rate of 0.1 s^{-1} was close to the experimental forging speed, the predicted damage evolution at the strain rate of 0.1 s^{-1} was used for comparison with the forging experiments. It should be noted that the measured damages (i.e., VFMV) by CT scanning were only obtained from the preform and the final forged components (see the scatter points in Fig. 16). However, the predicted damage (i.e., SDV4) can be recorded at each increased strain interval, thus the curves of damage evolution were

plotted. The results showed that the damage evolution under compression was increased very slowly; even the compressive strain increased to 0.7. On the other hand, the damage under tension increased rapidly to 0.00103 and 0.00136 at a tensile strain of 0.25 for SS316L and Ti-6Al-4V respectively, which was much greater than for the compressive deformation. Therefore, it can be concluded that only the tensile deformation would cause the final failure/fracture of the material due to damage accumulation. These predicted results were found to match quite well with the findings acquired from CT images after scanning as well as construction and detection sequentially.

Furthermore, the damage evolution of the RVE models at different strain rates was analysed for these two materials, as shown in Fig. 17. It can be seen that the strain rate had little influence on the damage evolution under compressive deformation. However, a significant rate-dependent effect was observed under tensile deformation for these two materials, i.e., the higher the strain rate, the faster the damage evolution at the same strain level.

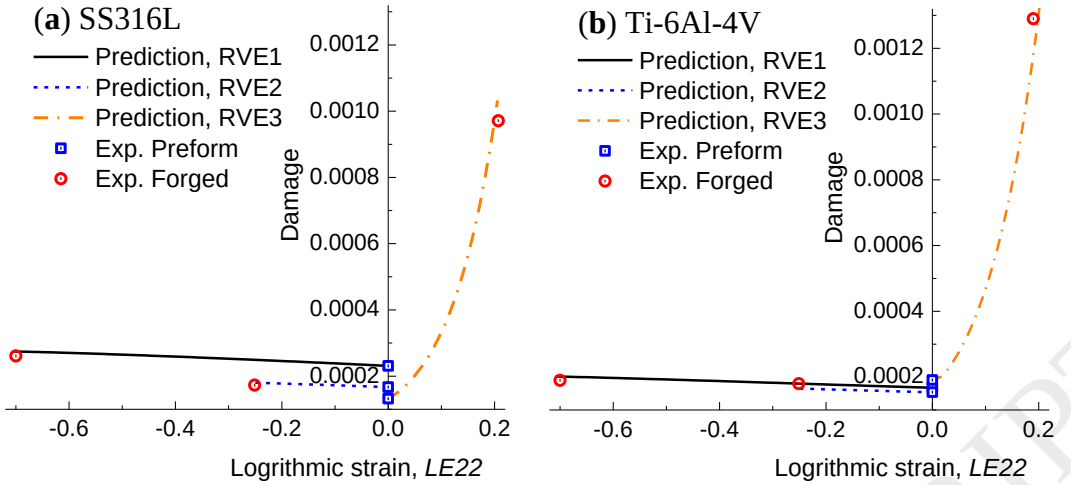

Fig. 16. Damage evolutions at different strain levels of the RVE models with various micro-voids for (a) SS316L and (b) Ti-6Al-4V.

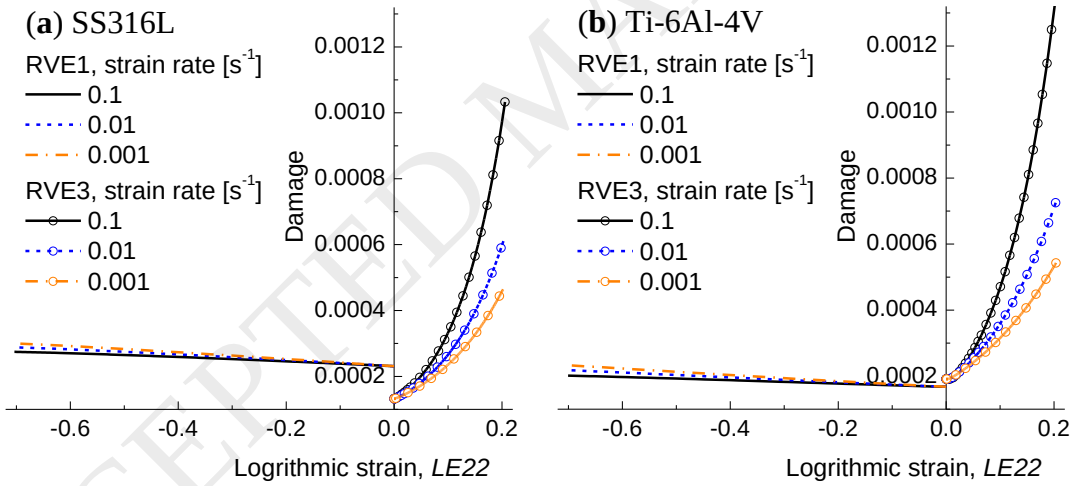

Fig. 17. Predicted damage evolutions of the RVE models with various micro-voids at different strain rates for (a) SS316L and (b) Ti-6Al-4V.

5. Conclusions

In this study, the micro-void evolution in warm-forging biocompatible alloys was quantified for damage prediction using 3D X-ray CT and RVE approach. Biocompatible alloys SS316L and Ti-6Al-4V were used as specimen materials in warm-forging a basal thumb implant. A micro-focus X-ray CT system was employed for scanning of both the preforms and forged components, and the 3D micro-void distribution and evolution inside the materials were detected and analysed quantitatively. RVE models were established for both SS316L and Ti-6Al-4V preforms; their localized damage distributions were predicted using an improved thermo-mechanical coupled micro-damage model and verified finally. The following conclusions can be drawn:

1. The stress-strain curves of cast SS316L at 800 ºC and Ti-6Al-4V at 700 ºC were obtained through uniaxial compression tests. The results indicated that the strain rate had little influence on the elastic modulus of the material. However, a significant rate effect was found on the plastic deformation behaviour in both SS316L and Ti-6Al-4V, i.e., the increasing strain rate led to significant increases in the yield and ultimate stresses of the material.
2. X-ray CT scanning demonstrated that the size distribution of the cast SS316L and Ti-6Al-4V preforms were similar, i.e., the sizes of the micro-voids inside the SS316L preform ranged from 22.2μm to 68.9μm with an average size of 33.5μm, and most of the micro-voids (approx. 87.7%) were sized between 28.7μm and 41.8μm, while the sizes of the micro-voids inside the Ti-6Al-4V preform ranged from 23.4μm to 67.0μm with an average size of 33.3μm, and most of the micro-

voids (approx. 91.3%) were sized between 24.5μm and 41.5μm. On the other hand, the micro-void distributions of the forged SS316L and Ti-6Al-4V components were quite different. For SS316L, the small-sized micro-voids (i.e., <24.4μm) were healed and medium-sized micro-voids (i.e., 37.5μm ~ 43.4μm) were increased after warm forging. For Ti-6Al-4V, the size of most micro-voids was reduced and the number of small-sized micro-voids was increased after warm forging.

3. The predicted damage evolution in the RVE models showed that the more severe damage was always distributed around the micro-voids, and the elements with more severe damage were less in both low and high compressive strain levels, as well as increasing a lot in tensile strain conditions. This indicated that the damage evolved very slowly under compressive deformation, while it grew quickly under tensile deformation.
4. The predicted damage under compression increased very slowly; even the compressive strain increased to 0.7. On the other hand, the damage under tension increased rapidly to 0.00103 and 0.00136 at a tensile strain of 0.25 for SS316L and Ti-6Al-4V respectively. Therefore, it can be concluded that only the tensile deformation would cause the final failure/fracture of the material due to damage accumulation. These predicted results were found to match quite well with the findings acquired from CT images after scanning as well as construction and detection sequentially. Thus, the application of non-destructive X-ray CT measurement of micro-voids incorporating the RVE approach was able to play a significant role leading to a more reliable damage prediction in the warm forging

process.

Acknowledgments

The work described in this paper was partially supported by a grant from the Research Committee of The Hong Kong Polytechnic University under student account code RTBN and a grant from the Research Grants Council of the Hong Kong Special Administrative Region, China (Project No. PolyU 511511). The authors would like to acknowledge Dr. Y.L. Zhu for FE modelling assistance.

References

Beal, J.D., Boyer, R., Sanders, D., 2006. Forming of titanium and titanium alloys. Metalworking: Sheet Forming (ASM Handbook), 14: 656-669.

Boljanovic, V., 2009. Metal shaping processes: casting and molding, particulate processing, deformation processes, and metal removal. Industrial Press Inc., New York.

British Stainless Steel Association, 2016. Elevated temperature physical properties of stainless steels. http://www.bssa.org.uk/topics.php?article=139.

Chan, L.C., Lu, X.Z., Yu, K.M., 2015. Multiscale approach with RSM for stress–strain behaviour prediction of micro-void-considered metal alloy. Mater. Des. 83, 129-137. https://doi.org/10.1016/j.matdes.2015.05.064.

Chen, M.S., Lin, Y.C., 2013. Numerical simulation and experimental verification of void evolution inside large forgings during hot working. Int. J. Plast. 49, 53-70. http://dx.doi.org/10.1016/j.ijplas.2013.02.017.

Coleman, B.D., Noll, W., 1963. The thermodynamics of elastic materials with heat conduction and viscosity. Arch. Ration. Mech. Anal. 13, 167-178.

https://doi.org/10.1007/BF01262690.

Feng, C., Cui, Z.S., Liu, M.X., Shang, X.Q., Sui, D.S., Liu, J., 2016. Investigation on the void closure efficiency in cogging processes of the large ingot by using a 3-D void evolution model. J. Mater. Process. Technol. 237, 371-385. https://doi.org/10.1016/j.jmatprotec.2016.06.030.

Geers, M.G., Kouznetsova, V.G., Brekelmans, W.A.M., 2010. Multi-scale computational homogenization: Trends and challenges. J. Comput. Appl. Math. 234, 2175-2182. https://doi.org/10.1016/j.cam.2009.08.077.

Gitman, I.M., Askes, H., Sluys, L.J., 2007. Representative volume: Existence and size determination. Eng. Fract. Mech. 74, 2518-2534. https://doi.org/10.1016/j.engfracmech.2006.12.021.

Gurson, A.L., 1977. Continuum theory of ductile rupture by void nucleation and growth: Part I—Yield criteria and flow rules for porous ductile media. J. Eng. Mater. Technol. 99, 2-15. https://doi.org/10.1115/1.3443401.

Hsieh, J., 2009. Computed tomography: principles, design, artifacts, and recent advances. Bellingham, WA: SPIE.

Ishikawa, T., Yukawa, N., Yoshida, Y., Tozawa, Y., 2005. Analytical approach to elimination of surface micro-defects in forging. CIRP Ann-Manuf. Technol. 54, 249-252. https://doi.org/10.1016/S0007-8506(07)60095-X.

Kaye, M., Puncreobutr, C., Lee, P.D., Balint, D.S., Connolley, T., Farrugia, D., Lin, J., 2013. A new parameter for modelling three-dimensional damage evolution validated by synchrotron tomography. Acta Mater. 61, 7616-7623. https://doi.org/10.1016/j.actamat.2013.08.065.

Lee, Y.S., Lee, S.U., Van Tyne, C.J., Joo, B.D., Moon, Y.H., 2011. Internal void closure during the forging of large cast ingots using a simulation approach. J. Mater. Process. Technol. 211, 1136-1145. https://doi.org/10.1016/j.jmatprotec.2011.01.017.

Lian, J.H., Yang, H.Q., Vajragupta, N., Muenstermann, S., Bleck, W., 2014. A method to quantitatively upscale the damage initiation of dual–phase steels under various stress states from microscale to macroscale. Comp. Mater. Sci. 94, 245-257.

https://doi.org/10.1016/j.commatsci.2014.05.051.

Lu, X.Z., Chan, L.C., 2017. Micromechanics-based damage model for failure prediction in cold forming. Mater. Sci. Eng. A 690, 120-131. https://doi.org/10.1016/j.msea.2017.02.069.

Malcher, L., Andrade Pires, F.M., César de Sá, J.M.A., 2014. An extended GTN model for ductile fracture under high and low stress triaxiality, Int. J. Plast. 54, 193-228, https://doi.org/10.1016/j.ijplas.2013.08.015.

Marshall, A., Ries, M.D., Paprosky, W., 2008. How prevalent are implant wear and osteolysis, and how has the scope of osteolysis changed since 2000? J. Am. Acad. Orthop. Surg. 16, S1-S6. http://dx.doi.org/10.5435/00124635-200800001-00003.

Matouš, K., Geers, M.G., Kouznetsova, V.G., Gillman, A., 2017. A review of predictive nonlinear theories for multiscale modeling of heterogeneous materials. J. Comput. Phys. 330, 192-220. https://doi.org/10.1016/j.jcp.2016.10.070.

Matula, M., Hyspecka, L., Svoboda, M., Vodarek, V., Dagbert, C., Galland, J., Stonawska, Z., Tuma, L., 2001. Intergranular corrosion of AISI 316L steel. Mater. Charact. 46, 203-210. https://doi.org/10.1016/S1044-5803(01)00125-5.

Momeni, A., Abbasi, S.M., 2010. Effect of hot working on flow behavior of Ti–6Al–4V alloy in single phase and two phase regions. Mater. Des. 31, 3599-3604. https://doi.org/10.1016/j.matdes.2010.01.060.

Pardoen, T., Hutchinson, J.W., 2000. An extended model for void growth and coalescence. J. Mech. Phys. Solids 48, 2467-2512. https://doi.org/10.1016/S0022-5096(00)00019-3.

Park, N.K., Yeom, J T., Na, Y. S., 2002. Characterization of deformation stability in hot forging of conventional Ti–6Al–4V using processing maps. J. Mater. Process. Technol. 130, 540-545. https://doi.org/10.1016/S0924-0136(02)00801-4.

Rosakis, P., Rosakis, A., Ravichandran, G., Hodowany, J., 2000. A thermodynamic internal variable model for the partition of plastic work into heat and stored energy in metals. J. Mech. Phys. Solids 48, 581-607. https://doi.org/10.1016/S0022-5096(99)00048-4.

Rousselier, G., 2001. Dissipation in porous metal plasticity and ductile fracture. J.

Mech. Phys. Solids 49, 1727-1746. https://doi.org/10.1016/S0022-5096(01)00013-8.

Sheljaskov, S., 1994. Current level of development of warm forging technology. J. Mater. Process. Technol. 46, 3-18. https://doi.org/10.1016/0924-0136(94)90099-X.

Shen, J., Mao, J.H, Reyes, G., Chow, C.L., Boileau, J., Su, X.M., Wells, J.M., 2009. A multiresolution transformation rule of material defects. Int. J. Damage Mech. 18, 739-758. https://doi.org/10.1177/1056789509346693.

Soyarslan, C., Turtuk, I.C., Deliktas, B., Bargmann, S., 2016. A thermomechanically consistent constitutive theory for modeling micro-void and/or micro-crack driven failure in metals at finite strains. Int. J. Appl. Mech. 8, 1650009, https://doi.org/10.1142/S1758825116500095.

Swanson, A.B., 2016. SWANSON Basal Thumb Implant. http://www.wmtemedia.com/ProductFiles/Files/PDFs/014493_EN_LR_LE.pdf.

Tvergaard, V., Needleman, A., 1984. Analysis of the cup-cone fracture in a round tensile bar. Acta Metallurgica 32, 157-169. https://doi.org/10.1016/0001-6160(84)90213-X.

Veiga, C., Davim, J.P., Loureiro, A.J.R., 2012. Properties and applications of titanium alloys: a brief review. Rev. Adv. Mater. Sci. 32, 133-148.

Xiao, H., Bruhns, O.T., Meyers, A., 2007. Thermodynamic laws and consistent Eulerian formulation of finite elastoplasticity with thermal effects. J. Mech. Phys. Solids 55, 338-365. https://doi.org/10.1016/j.jmps.2006.07.005.

Zhao, P.J., Chen, Z.H., Dong, C.F., 2016. Experimental and numerical analysis of micromechanical damage for DP600 steel in fine-blanking process. J. Mater. Process. Technol. 236, 16-25. http://dx.doi.org/10.1016/j.jmatprotec.2016.05.002.

Zhao, P.J., Chen, Z.H., Dong, C.F., 2016. Failure analysis based on microvoids damage model for DP600 steel on in-situ tensile tests. Eng. Fract. Mech. 154, 152-168. https://doi.org/10.1016/j.engfracmech.2015.11.017.

Zhu, Y.L., Kang, G.Z., Kan, Q.H., Bruhns, O.T., Liu, Y.J., 2016. Thermo-mechanically coupled cyclic elasto-viscoplastic constitutive model of metals: Theory and application, Int. J. Plast. 79, 111-152. https://doi.org/10.1016/j.ijplas.2015.12.005.

Figure Caption

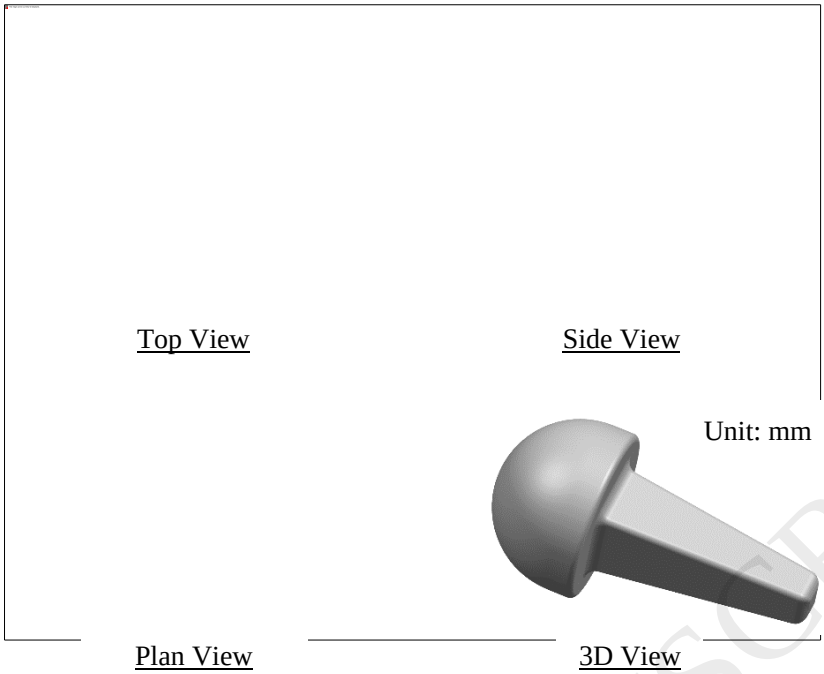

Fig. 1. The final configuration of a basal thumb implant in this study.

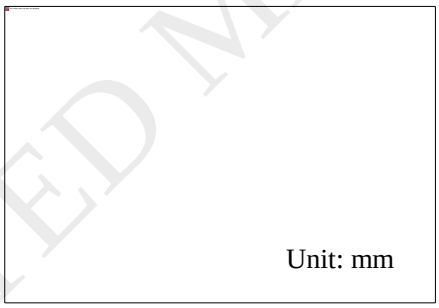

Fig. 2. The current design of the basal thumb implant preform.

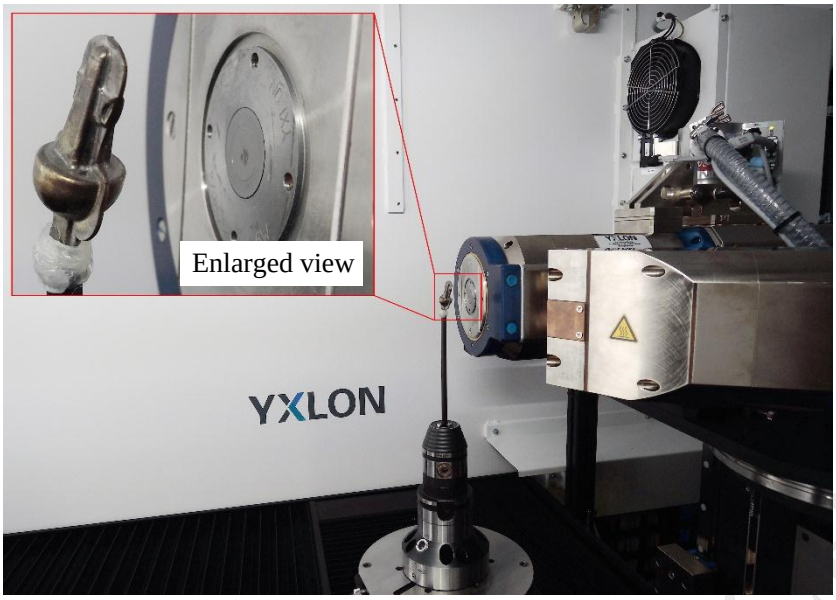

Fig. 3. X-ray CT scanning of the forged basal thumb component.

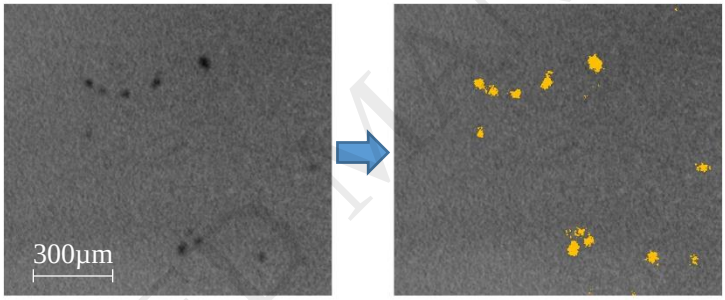

Fig. 4. Micro-voids detection: Original CT images on LHS; Constructed micro-voids in yellow via VGStudio on RHS.

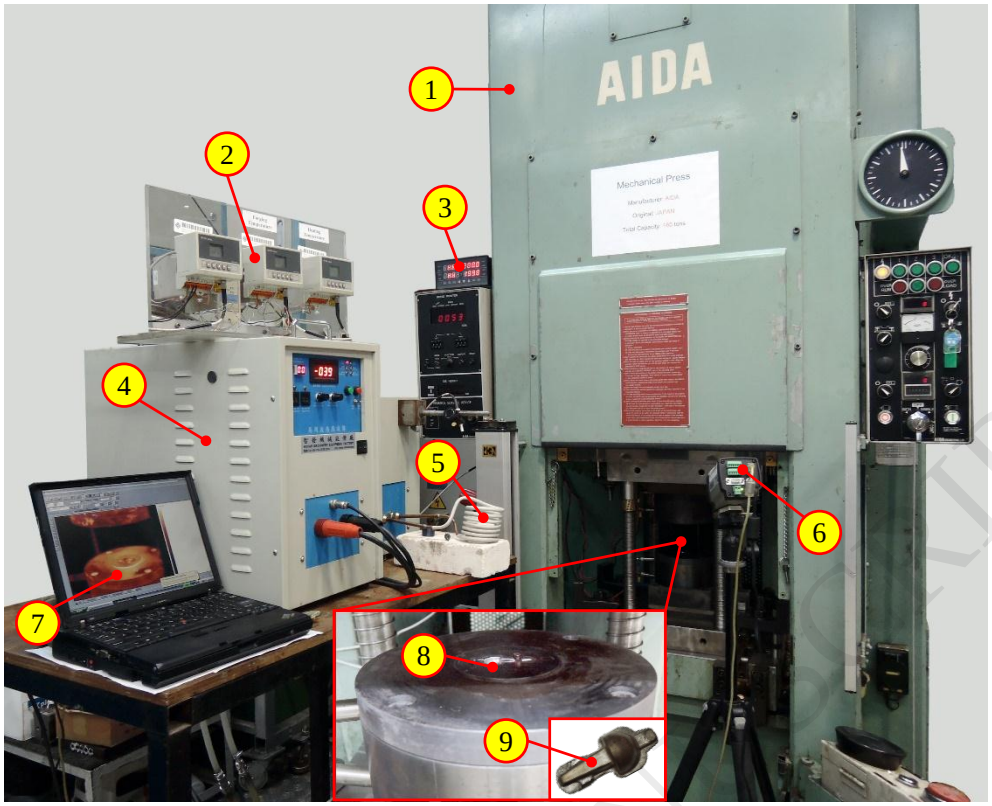

Fig. 5. A self-developed experimental system for warm-forging the basal thumb implant. Note: 1. 160T AIDA mechanical press; 2. Displays of the infrared thermometers for preform temperature measurement and monitoring; 3. Temperature monitor and controller for the forging die; 4. Induction heating equipment; 5. Preform inside the heating coil; 6. Infrared thermal camera; 7. Real-time temperature distribution during forging; 8. Bottom die core; 9. Forged component.

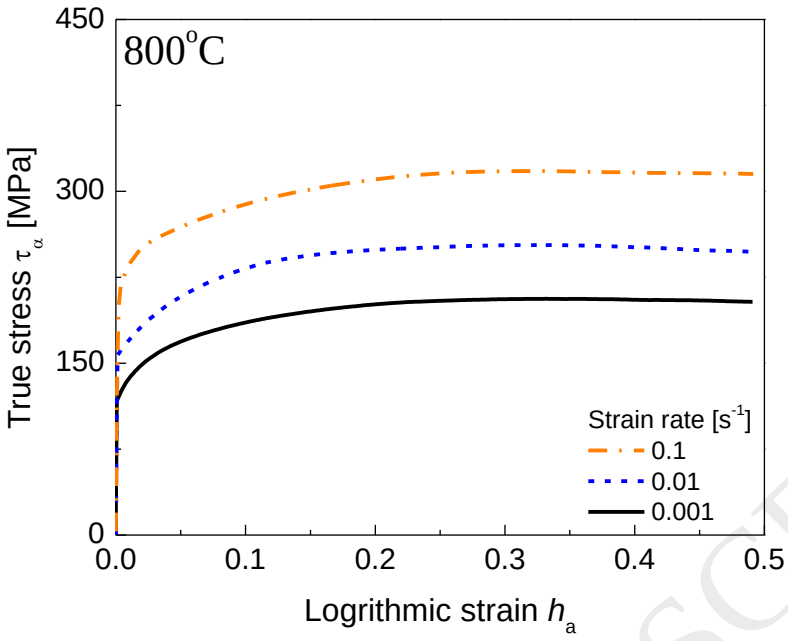

Fig. 6. Experimental compressive stress-strain curves of the SS316L specimens at elevated temperature of 800 ºC.

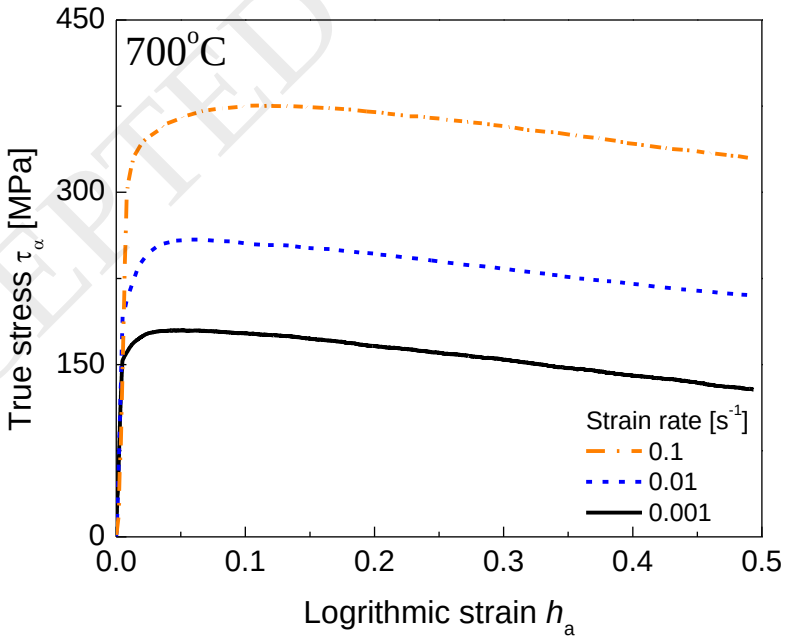

Fig. 7. Experimental compressive stress-strain curves of the Ti-6Al-4V specimens at elevated temperature of 700 ºC.

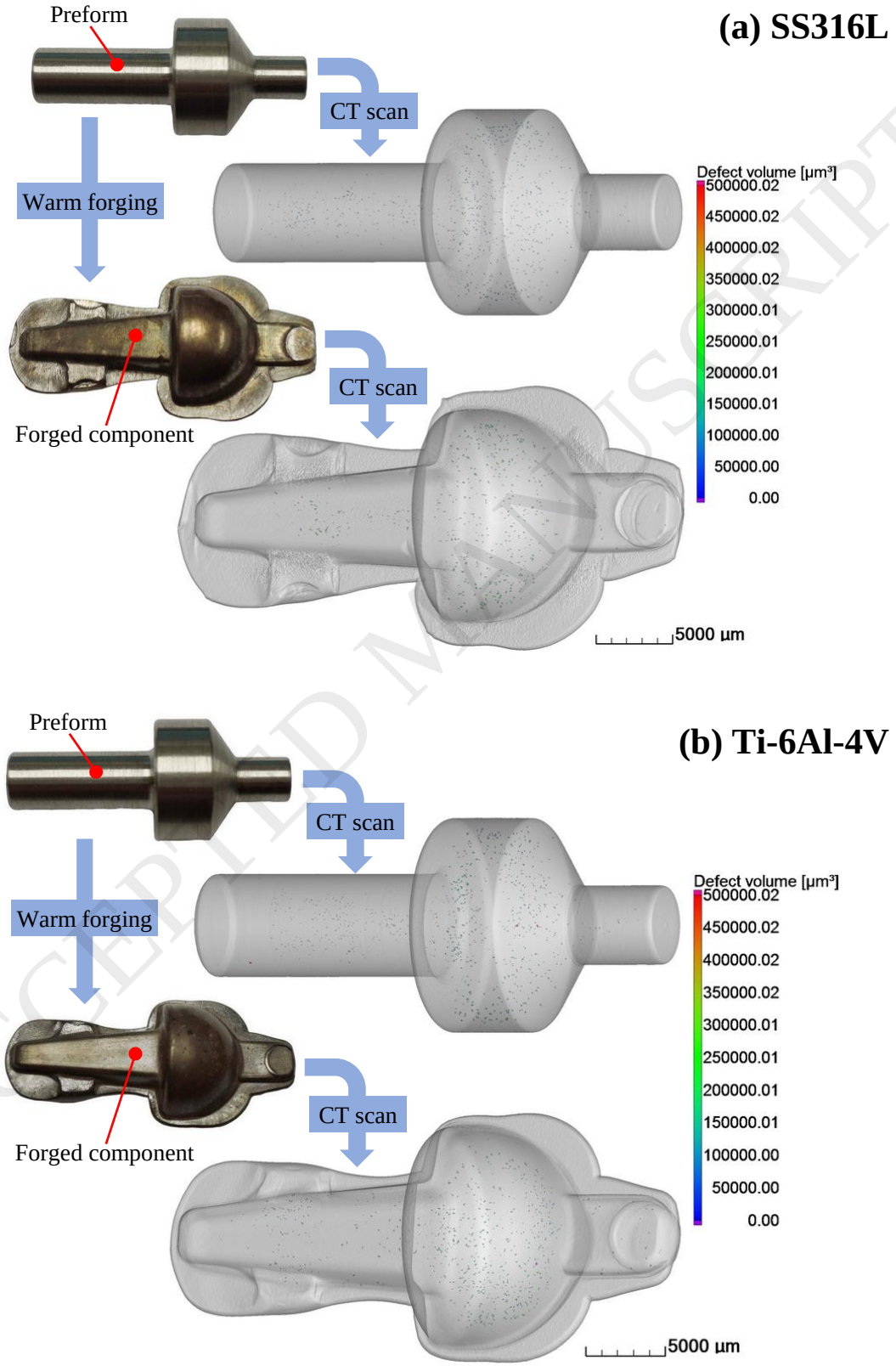

Fig. 8. The experimental preforms and forged components as well as their 3D CT images with internal micro-voids to be illustrated on (a) SS316L and (b) Ti-6Al-4V.

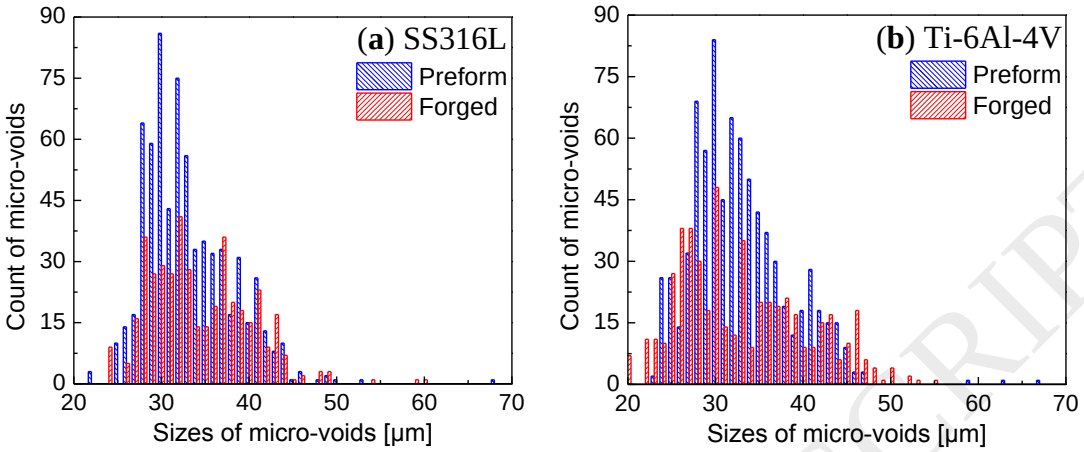

Fig. 9. Sizes distribution of micro-voids in: (a) SS316L and (b) Ti-6Al-4V.

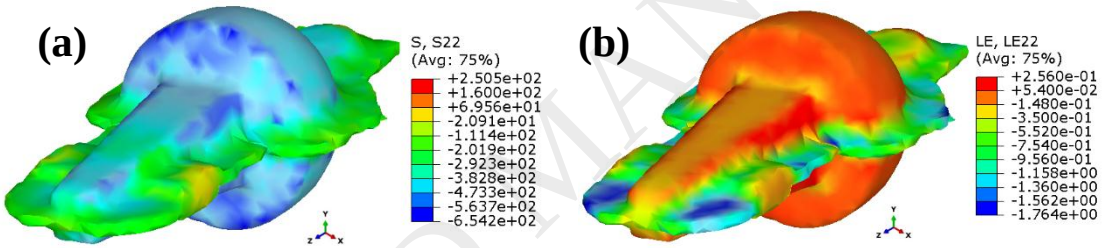

Fig. 10. The predicted stress distribution (a) and strain distribution (b) of the forged SS316L basal thumb component.

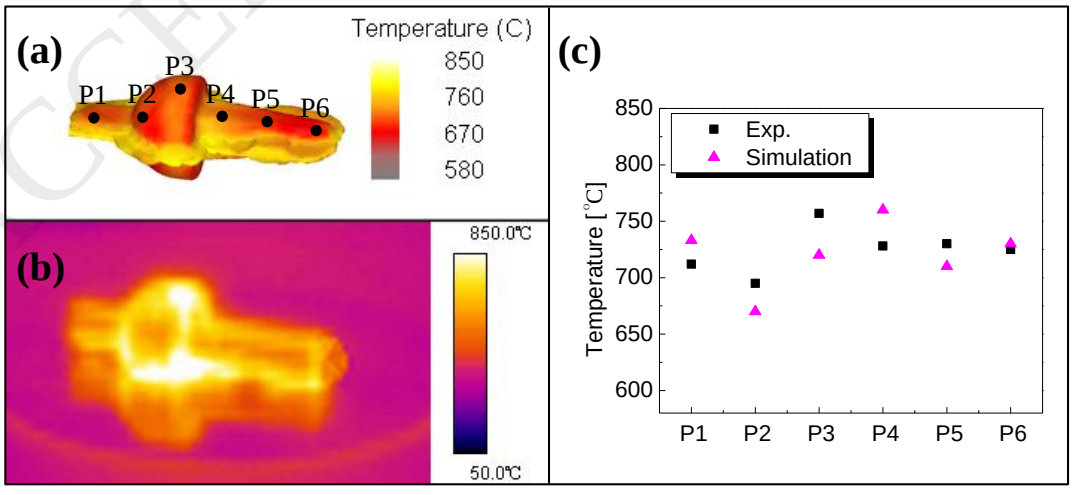

Fig. 11. Comparison of temperature distributions between (a) prediction and (b) thermal camera capturing image of the forged SS316L component, as well as (c) temperature comparison of selected feature points.

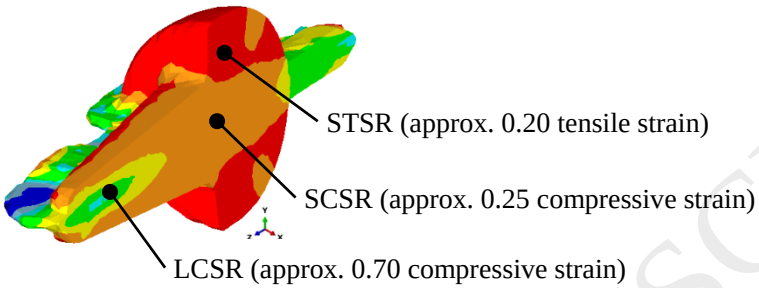

Fig. 12. Three typical strain regions of the forged SS316L basal thumb component: STSR, SCSR and LCSR.

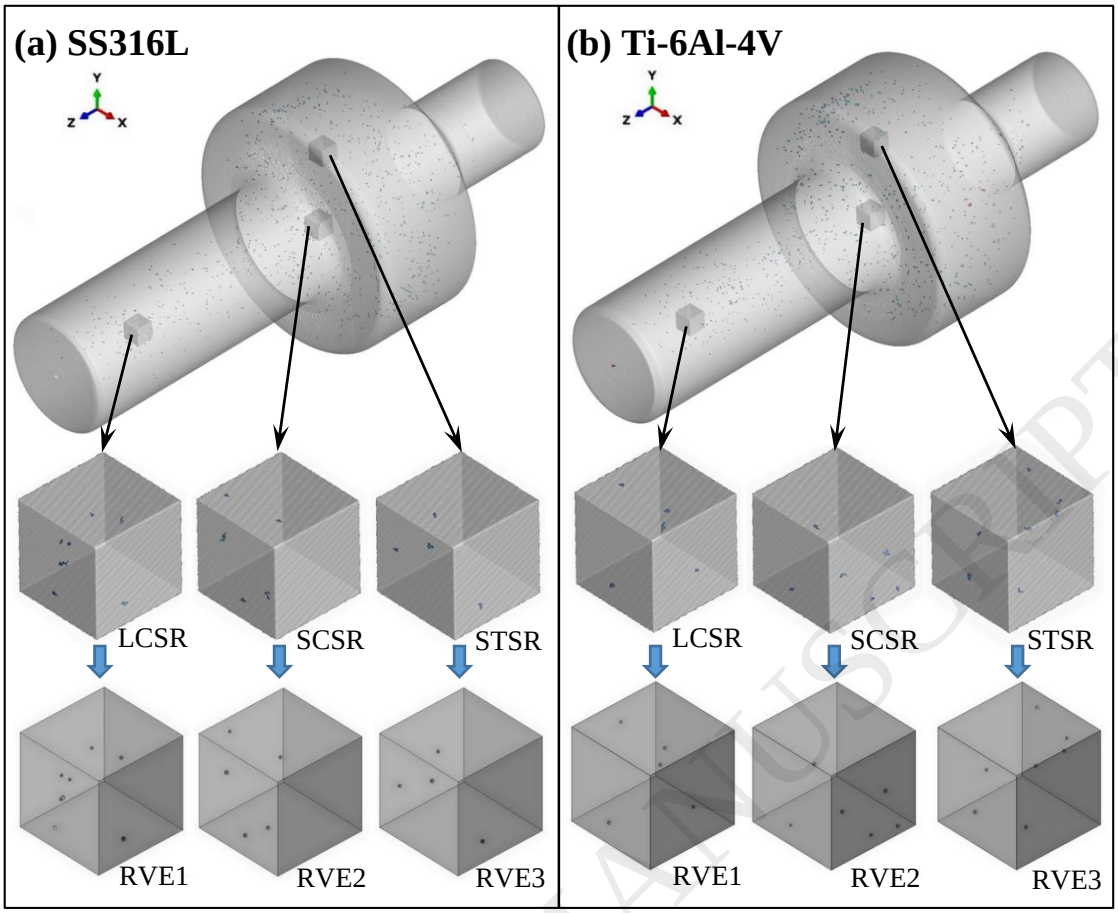

Fig. 13. RVE models (1.0mm in side length) constructed after CT scanning of the preforms: (a) SS316L and (b) Ti-6Al-4V.

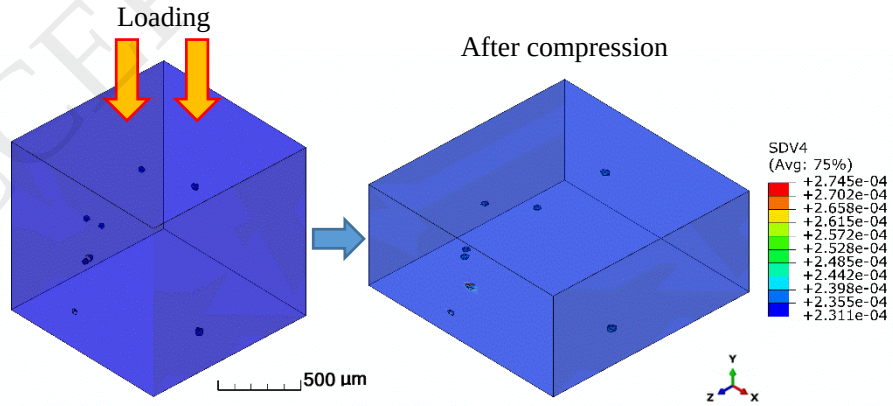

Fig. 14. Predicted damage distribution of RVE1 for SS316L (800 ºC, 0.1 s^{-1} strain rate, at strain of -0.70 (*LE22*)).

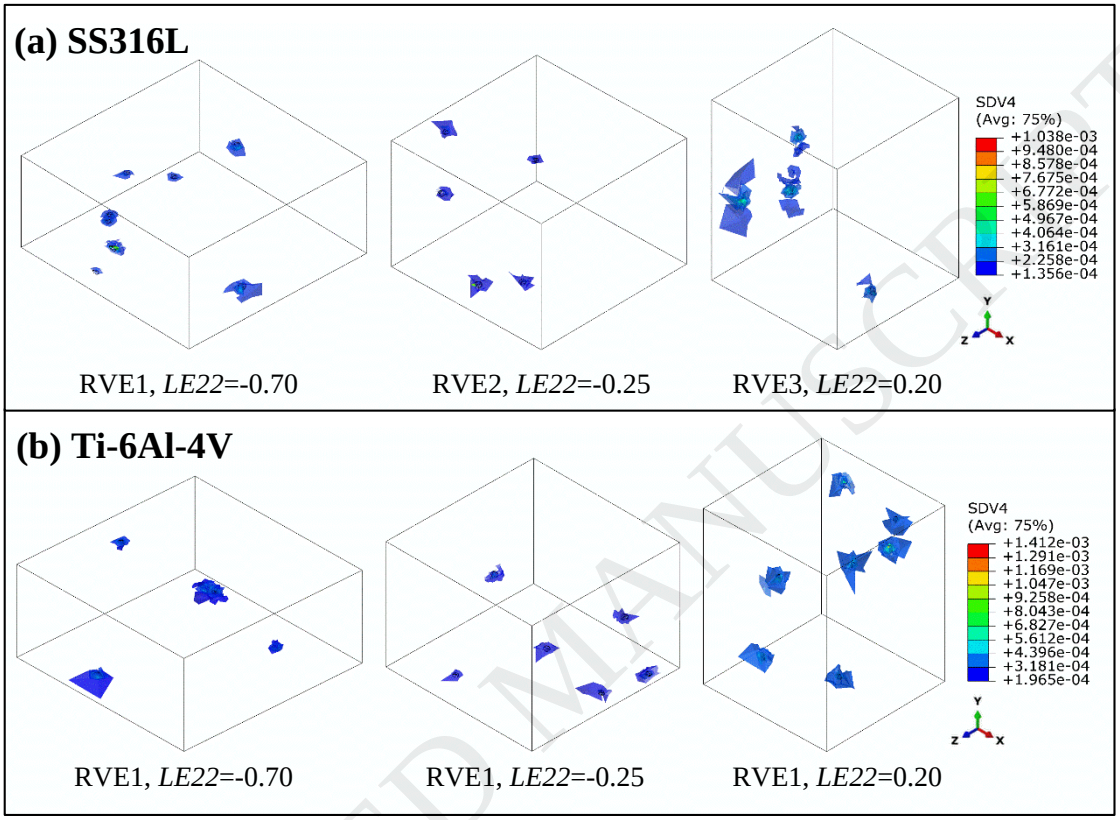

Fig. 15. Damage localization around the micro-voids in RVE models of (a) SS316L and (b) Ti-6Al-4V.

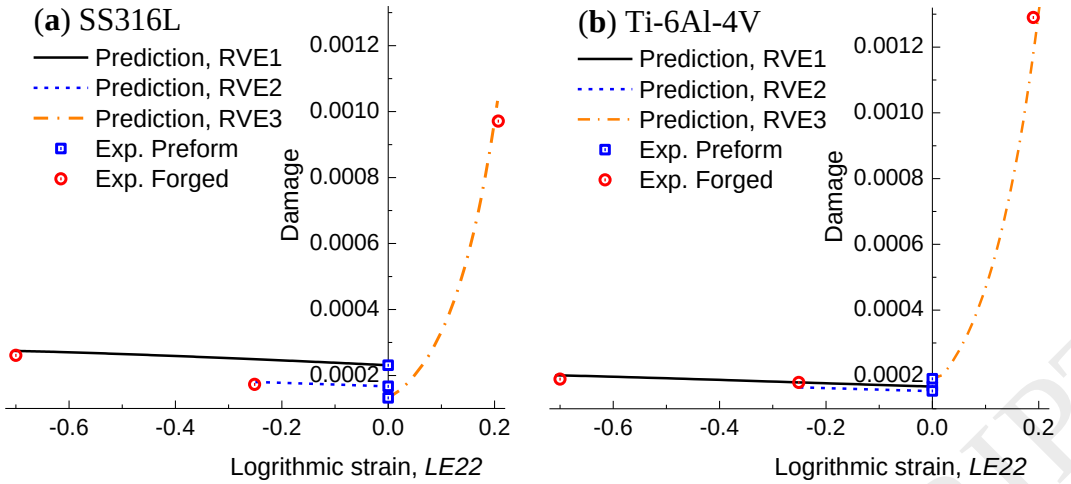

Fig. 16. Damage evolutions at different strain levels of the RVE models with various micro-voids for (a) SS316L and (b) Ti-6Al-4V.

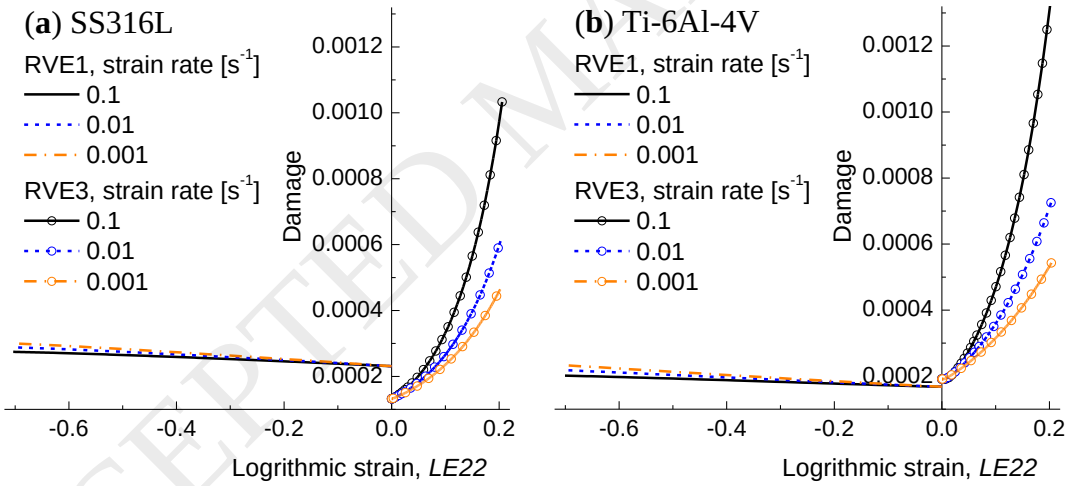

Fig. 17. Predicted damage evolutions of the RVE models with various micro-voids at different strain rates for (a) SS316L and (b) Ti-6Al-4V.

Table 1

Chemical composition (% in mass) of SS316L in this study.

C	Mn	S	Si	Cr	Ni	Mo	Fe
0.024	1.68	0.003	0.03	16.73	11.55	1.52	balance

Table 2

Chemical composition (% in mass) of Ti-6Al-4V in this study.

C	O	Fe	Al	V	Ti
0.03	0.03	0.25	6.22	4.15	balance

Table 3

Material parameters of SS316L (at 800 ºC) and Ti-6Al-4V (at 700 ºC) to be involved in the formulation of thermo-mechanical coupled micro-damage model.

	E (GPa)	ν	Q_0 (MPa)	R^{sat1} (MPa)	R^{sat2} (MPa)	β_1	β_2	K	n	s_1	s_2	c (J/kg.K)	k (W/m·K)
SS316L	134	0.24	120	84.7	/	16.5	/	300	6	2	200	628	21.0
Ti-6Al-4V	32	0.34	150	37.2	174	78.8	-0.6	500	5	2	235	750	14.6